UNIVERSITY OF CALIFORNIA

SANTA CRUZ

RETINAL RESPONSES TO STIMULATION WITH A PHOTOVOLTAIC PROSTHESIS

A dissertation submitted in partial satisfaction of the requirements for the degree of

DOCTOR OF PHILOSOPHY

in

PHYSICS

by

Richard Smith

December 2016

The Dissertation of Richard Smith is approved:

_____

Professor Alexander Sher,
Chair

_____

Professor Bruce Schumm

_____

Professor Joshua Deutsch

_____

Professor David Feldheim

_____

Dean Tyrus Miller
Vice Provost and Dean of Graduate Studies

Contents

List of Figures

List of Tables

The text of this dissertation includes partial reprints of the following previously published material. The co-authors approved of its inclusion in this dissertation. The sections and figures that came from these papers are indicated with footnotes.

[23] Goetz, G., Smith, R., Lei, X., Galambos, L., Kamins, T., Mathieson, K., Sher, A., and Palanker, D. Contrast Sensitivity With a Subretinal Prosthesis and Implications for Efficient Delivery of Visual Information. Invest Ophthalmol Vis Sci. (2015), 56(12): 7186-94

[37] Lorach, H., Goetz, G., Smith, R., Lei, X., Mandel, Y., Kamins, T., Mathieson, K., Huie, P., Harris, J., Sher, A., and Palanker, D. Photovoltaic restoration of sight with high visual acuity. Nat. Medicine (2015).

[44] Mathieson, K., Loudin, J., Goetz, G., Huie, P., Wang, L., Kamins, T. I., Galambos, L., Smith, R., Harris, J. S., Sher, A., and Palanker, D. Photovoltaic retinal prosthesis with high pixel density. Nat. Photonics 6, 6 (2012), 391-397.

[58] Smith, R., Goetz, G., Ho, E., Lei, X., Galambos, L., Kamins, T., Mathieson, K., Palanker, D, and Sher, A. Spatio-temporal characteristics of retinal response to network-mediated photovoltaic stimulation. Currently in submission process to J Neurophysiology.

Abstract

Richard Smith

Retinal Responses to Stimulation with a Photovoltaic Prosthesis

Here we present the design and characterization of a fully wireless subretinal visual prosthesis, which delivers electrical stimulation via photovoltaic pixels, illuminated with pulsed near infrared light (880-915 nm). In this dissertation I characterize the retinal responses to this photovoltaic retinal prosthesis in-vitro. The results show that the devices preserve crucial features of natural vision, including adaptation to static visual scenes, flicker fusion, and transient responses to changes in luminance. Arrays comprised of hexagonal pixels that are each either 140 μm or 70 μm wide safely elicit retinal responses in-vitro, as well as cortical responses in-vivo, in both healthy and diseased animal models. The stimulation takes advantage of the existing retinal network and is highly localized, restoring vision in blind rats at up to half the normal visual acuity. The retina is able to respond to high-frequency stimulation (20Hz), approaching that of natural visual scenes, surpassing other retinal prostheses that fail to reliably produce visual responses above 7Hz. The ability of this device to reliably produce retinal responses to high-frequency images is a promising indication of a new level of patient satisfaction that might be obtained during the first human clinical trials taking place later this year.

Acknowledgements

First of all I would like to thank my advisor, Alexander Sher. I have long been fascinated by neuroscience and I am grateful to have had the opportunity to explore this field from within the physics department. Professor Sher demonstrated great leadership skills and has helped nurture a creative, methodical and effective inquisitive process.

I would like to give thanks for the music and dance community of Santa Cruz, which has greatly shaped and changed me over these last six years. Several my fellow physics graduate students have been unexpectedly and especially influential in exploring the realms of art, music and nature together, including Trevor Keiber, Andrew Marsh, Angelo Monteux, Gregory Kaminsky. Their friendship has provided a catalyst for growth beyond the lab and has been an immeasurable source of intellectual and emotional support. Other friends from the community who have contributed enormously to my health, well being, and personal growth over the last six years include Daniel Weisberg, Lauren Ford, Pia Litz, Kelsey Forest, Dan Nazarian, Lauren Henry, my brother Ernie, and Ancestree Reggae: Tomás Gomez, Tom Maimon, Chris Carr, Alia Fintz, Judd DiSalvo, and David Goodman.

I would like to thank the taxpayers of the state of California, and especially progressive voters who believe that education is a worthwhile investment, and are interested in putting our collective resources towards educating the youth.

Many rats were sacrificed for this work, in order to restore vision to humans. I give thanks to all of the creatures who unwillingly participated in these experiments, and I urge scientists everywhere to have the utmost respect for all life and to only use the bare minimum number of creatures necessary, and for only the most crucial work.

Our partner lab at Stanford University, run by Professor Daniel Palanker's exemplary leadership, has been a crucial part of my dissertation work and I would like to thank all of their members who contributed to this project, especially Georges Goetz with whom I spent many long hours in a very dark room. His buoyant attitude even in the face of many failed experiments helped immensely, as did his thorough and attentive scientific nature. Thanks to Keith Mathieson who helped me in my early days of adjusting to this project. Thanks to Sergei Kachiguin for always being able to discover the source of hardware and technical problems. Thanks to other members of the Sher/Feldheim lab for various types of help including Shinya Ito, Corrine Beier, Erin Zampaglione, Jimmy Shanks, and Anahit Hovhannisyan.

Lastly I would like to thank my parents and grandparents who brought me into the world.

Chapter 1: Introduction

1.1 Motivation

Degeneration of the retina through diseases such as age-related macular degeneration and retinitis pigmentosa is the leading cause of untreatable blindness (57). In such diseases, the progressive degeneration of the image-capturing photoreceptors leads to a gradual loss of the eye's ability to translate visual information into neural signals. However, the image-processing layers of retina beneath the photoreceptors are usually relatively well preserved (46) even in later stages of such degenerative diseases. Retinal prostheses take advantage of this intact retinal infrastructure and seek to restore sight by electrically stimulating these surviving neurons.

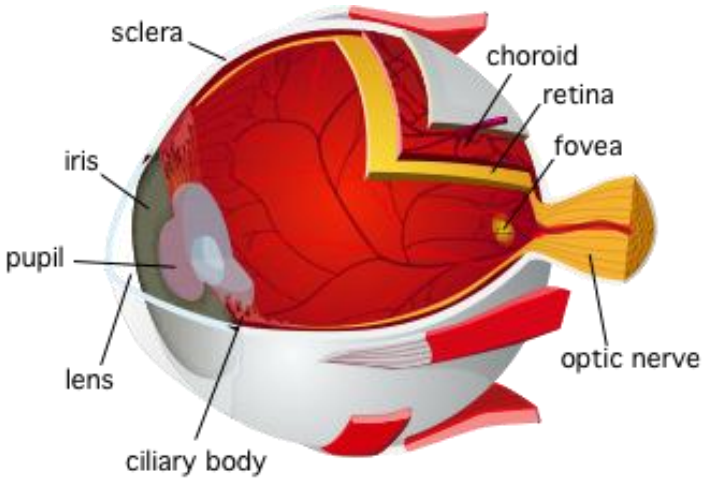

Figure 1.1 Schematic of the eye. *Image by Ignacio Icke, Creative Commons license.*

Several types of retinal implants have been proved to reliably elicit percepts of light in blind patients, but they suffer from a number of problems. Most of these use bulky power cables and intraocular electronics that are cumbersome to implant such as the ARGUS II epiretinal implant from Second Sight Inc. Visual percepts are often distorted, with low spatial resolution and a very limited number of perceivable gray levels (1, 13).

The wireless subretinal photovoltaic prosthesis that we examine here is markedly improved on the other visual prostheses in its class in a number of ways, including the ability to deliver high-frequency stimuli, higher spatial resolution, and wireless functionality. This thesis focuses on the in-vitro characterization of the performance of a wireless subretinal photovoltaic prosthesis. The main goal of this research was to examine the performance of this prosthesis *in-vitro* and compare it to other retinal prostheses as well as to natural vision, in anticipation of human clinical trials. The work is supported by *in-vivo* studies conducted at Stanford University. This introductory chapter describes the neural circuitry of the mammalian retina and the details of the photovoltaic retinal prosthesis.

1.2 The nervous system

The nervous system is an interconnected network of cells that an animal uses to coordinate its voluntary and involuntary actions, and transmit information to different

parts of the body. The fundamental unit of this network, the neuron, is an electrically excitable cell that can transmit information to adjacent neurons through the use of electrical and chemical signals. Typically, each neuron has 3 main parts: the cell body, the dendrites, and the axon (Figure 1.2). The dendritic tree collects and integrates signals *from* a single neuron or up to 10,000 neurons. The axon transmits a processed signal from the cell body *to* another neuron (or neurons), at the axon terminal, where a *synapse* forms a functional connection between neurons via electrical or chemical signaling. Neural signals affect the voltage difference between the outside and inside of each neuron, called the membrane potential. Steady-state voltage gradients are maintained in each neuron by the use of metabolically driven ion pumps.

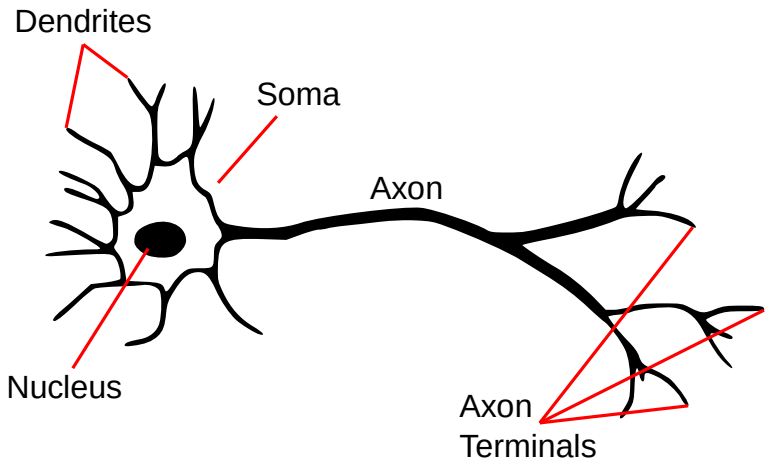

Figure 1.2 Schematic of a neuron. The connection between adjacent neurons occurs at the synapse, between the axon terminals of one neuron and the dendrites of the adjacent neuron. *Creative Commons license.*

The resting membrane potential of a neuron is usually about -70mV, compared to the extracellular medium. Embedded in the cell membrane are metabolically-driven ion

pumps which maintain trans-membrane concentrations of specific ions such as potassium, sodium, and calcium, which are used to create voltage gradients across the cell membrane. These ion pumps balance the flow of ions through voltage-controlled ion channels and ligand-controlled ion channels, the main sources of cell-to-cell communication. Andrew Huxley and Alan Lloyd Hodgkin were the first to explain the role of ions in cell membrane voltage fluctuations (27).

Ligands open and close ion channels through specific protein-binding mechanisms, and these ligands are known as *neurotransmitters*. When the voltage inside a cell rises in relation to the voltage outside the cell, the cell is becoming *depolarized*, which can lead to an *action potential*, an all-or-nothing event in which the voltage of a cell rises very quickly if a certain voltage threshold is surpassed (Figure 1.3). When the threshold is surpassed, voltage-gated ion channels open allowing an influx of positively-charged sodium ions into the cell, further driving up the voltage inside the cell. Shortly thereafter, voltage-gated potassium channels allow positively-charged potassium ions *out* of the cell, restoring the resting potential of the neuron. In this way, a large, fast voltage increase inside the cell is followed by a sharp decrease and return to baseline, allowing the cell to prepare for another action potential. Action potentials (or *spikes*) are the fundamental unit of neural communication, but are also supplemented by gap junctions which can transmit electrical current directly from cell-to-cell.

Excitatory neurotransmitters are responsible for rises in voltage fluctuation, whereas inhibitory neurotransmitters are responsible for a decrease in the cell's voltage. The trans-membrane potential of a neuron affects the rate of neurotransmitter release at the axon terminal, which in turn affects the trans-membrane potential of the neurons whose dendrites are in contact with that axon. For graded-response cells, the amount of neurotransmitter release can be a gradual modulation, whereas for spiking cells, the trans-membrane potential affects whether or not an action potential occurs. Either way, the trans-membrane electrical potential is the main source of cell-to-cell communication.

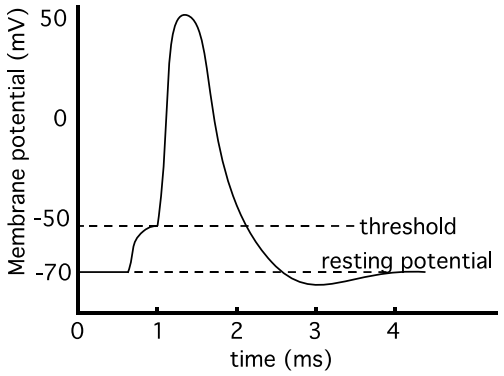

Figure 1.3 Action potential. When the voltage potential between the inside and the outside of a neuron exceeds a certain threshold value, voltage-gated ion channels open allowing an influx of positively-charged sodium ions into the cell, further driving up its potential. Shortly thereafter, voltage-gated potassium channels allow positively-charged potassium ions *out* of the cell, restoring the resting potential of the neuron.

Because electrical potential is the medium by which neurons communicate with each other, it is also the natural avenue by which researchers have long sought to control and modify sensory input and experience. One captivating early example was that of

18th century physicist Luigi Galvani causing dead frogs' legs to twitch with the application of electrical stimulation. More all-encompassing experiences, such as the vivid world inflicted upon subjects depicted in the 1999 movie, The Matrix, would be hard to achieve with external stimulation, but it is indeed theoretically possible: by stimulating the right neurons in the right way, any sensory experience is achievable.

Applications of electrical stimulation have many proven medical uses, from deep-brain stimulation to relieve aspects of Parkinson's disease, prosthetic limbs that actually respond to the original neural commands from the brain, and cochlear and retinal implants. It is possible both to read out, and to modify, neural activity. Recording electrodes are used in various applications for characterizing neural activity, and stimulating electrodes can be used to modify that activity by inducing action potentials in neurons. In the prosthesis presented in this dissertation, only stimulating electrodes are used, but in our in-vitro experiments, we use recording electrodes to identify neural activity in the retinal tissue while stimulating that same tissue with the prosthesis (see Methods).

1.3 Anatomy of the retina

The retina is one of the most accessible extensions of the nervous system, and has consequently been studied a great deal in the last several centuries. The retina consists of three layers of neurons: the photoreceptors, the inner nuclear layer, and the ganglion cell layer. The processing of visual information begins in the

photoreceptors, where incoming light has been focused and projected by the lens and cornea. In vertebrates, the photoreceptors are located at the back of the retina, such that incoming light passes through the other, transparent, layers of the retina before being absorbed.

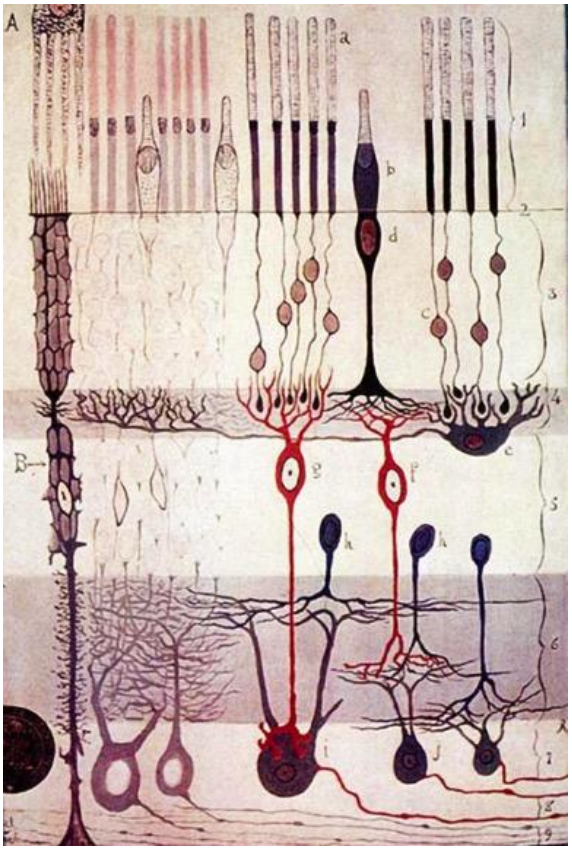

1.4 Early drawing of the retina. From "*Structure of the Mammalian Retina*" c.1900 by Santiago Ramon y Cajal, achieved with silver staining.

Photoreceptors are non-spiking neurons which change their membrane potential according to the number of photons they absorb, via the action of light-sensitive opsin proteins which open or close voltage-gated ion channels. Rod photoreceptors

are primarily responsible for low-light vision and cone photoreceptors are largely responsible for daytime and color vision. Primates and humans have 3 types of cone photoreceptors, called S, M, and L, corresponding to the short (419 nm), medium (531 nm), and longer (561 nm) wavelengths of light to which their opsin proteins are most sensitive. Through the interaction of signaling from these 3 cone subtypes, we experience our full range of color vision. The human retina has approximately 120 million photoreceptors, with the cones being located near the most dense part of the central retina, called the fovea, and the rods concentrated more around the periphery, (Figure 1.1) which is why we often have better night vision by directing our gaze slightly away from the object of interest.

The next layer of information encoding happens in the inner nuclear layer, where the photoreceptors relay their changes in membrane potential to 2 types of horizontal cells, about 12 types of bipolar cells, and perhaps as many as 30 types of amacrine cells (42), that integrate the photoreceptor signals in various ways before connecting to the next layer of ganglion cells. There are about 20 distinct types of ganglion cells. The axon of each ganglion cell travels all the way down the optic nerve to the brain. A great deal of visual processing occurs in the retina before the signals reach the brain: indeed it is an extension of the brain itself.

There are ganglion cells in rodents, for example, which are direction-selective, and only respond to motion in specific directions (2). In the primate retina the majority of the cells in this layer are various types of ON and OFF ganglion cells. The smallest

ones, called ON and OFF midget cells, are thought to be responsible for the high visual acuity in primates (48).

The receptive fields of different retinal ganglion cell (RGC) types form complementary mosaics over the retinal surface (18, 11, 20, 14, 64) and the network connectivity patterns within them define the characteristics of retinal processing. RGCs respond to changes in luminance by generating action potentials in response to light increments (ON- cells), or decrements (OFF- cells), or both increments and decrements in illumination (ON-OFF cells) (26). Each retinal ganglion cell is only sensitive to incoming light in a region of the retina called its receptive field. ON ganglion cells respond to increases in light in their receptive field, and OFF cells respond to decreases in light.

The primary signaling mechanisms between layers of the retina is the neurotransmitter *glutamate*. The signaling pathway begins at the photoreceptors, which *decrease* their rate of glutamate release upon receiving in an *increase* in the number of photons. ON and OFF bipolar cells respond oppositely to the presence of glutamate at their dendrites, by either increasing their rate of glutamate release at their connections with the ganglion cell layer (ON bipolar), or decreasing (OFF bipolar). ON and OFF RGCs are always depolarized by the presence of glutamate at their dendrites and thereby their axons, which travel all the way to the visual cortex, will convey whether the light in its receptive field has increased or decreased.

Horizontal cells connect laterally and compare adjacent regions of photoreceptors, with their axons connected to the output of adjacent photoreceptors to form a negative feedback network. In the center of each RGC's receptive field, a small group of photoreceptors are serviced by one or more horizontal cells which act in an opposing way on the photoreceptors surrounding that region. So, with an increase in light in the center region, the photoreceptors around it will adjust their rate of glutamate release as if they had received a decrease in light. This is accomplished by the release of GABA, an inhibitory transmitter, from the horizontal cell axons, onto adjacent photoreceptors (61). This mechanism enhances edges and creates better contrast recognition, and contributes to the *center-surround* organization of receptive fields.

In each case, the outer region of the receptive field is antagonistic, meaning that it responds to the opposite type of stimulus that the center of the receptive field responds to. For an ON RGC, its strongest stimulus would be a region that becomes brighter directly in the center of the receptive field, while the immediate area around it becomes darker.

The manner by which ganglion cells can respond to various specific stimuli is due to such mechanisms in the inner nuclear layer. Bipolar cells are largely responsible for the response of ganglion cells to the centers of their receptive fields, whereas horizontal cells, whose dendrites reach laterally over a larger area, help to mediate

surround effects through a negative feedback network at the photoreceptor level. Amacrine cells form lateral as well as stratified connections in the retina, and contribute to many different features of vision (43). The exact function of the different subtypes of bipolar cells cells, as well as the many amacrine cell types, is still a vigorously-studied area of vision science.

1.4 Retinal degeneration

Such a complex infrastructure of signaling begs the question: what chance do we have of repairing or replacing the retina when it fails in blindness? Fortunately, the most common types of blindness are degenerative retinal diseases that primarily affect the photoreceptors, leaving the inner nuclear layer and ganglion cell layer intact (41). Such a specific form of degeneration allows for the possibility of electrical stimulation, utilizing the existing retinal infrastructure to relay the signals to the brain. Age-related macular degeneration (AMD) is the most common of these degenerative diseases, affecting the photoreceptors in the fovea, usually in populations over 60 years of age. It is very hard for patients to read, recognize faces, or discern any significant visual details, even though their peripheral vision is relatively intact and often allows them to carry out tasks such as walking. On the other hand, Retinitis Pigmentosa (RP) begins by primarily affects photoreceptors in the peripheral visual field before moving inward, and occurs mostly in younger populations of about 20-30 years of age.

There are two types of AMD: wet and dry. With the progression of AMD, the retinal pigment epithelium (RPE) cells slowly deteriorate, leaving cellular debris called drusen which impedes the transport of nutrients from the choroid (57). In the dry form of AMD, the RPE cells located directly behind the fovea begin to atrophy. The photoreceptors in that area begin to die as a result, and the patient is left with a blind spot right in the middle of their visual field, called a scotoma. The less-common form of AMD is the wet version, which accounts for less than 10% of cases. Here, a process called neovascularization results in new blood vessels growing from the choroid into the retina, which causes the formation of a new membrane between the retina and the RPE, which cuts off nutrient flow also leads to photoreceptor death. Injectable anti-angiogenic drugs can block the growth factor responsible for the formation of these new blood vessels, but must be delivered on a monthly basis.

1.5: (a) A natural scene, with simulated effects of (b) Retinitis Pigmentosa (RP) and (c) Age-Related Macular Degeneration (AMD) on the visual field. (b) RP initially causes a loss of visual acuity in the periphery, resulting in tunnel vision in the later phases of the disease as schematically represented here by the blacked-out portion of the visual field. (c) AMD affects the central portion of the visual field. The disappearance of photoreceptors around the fovea makes it difficult for patients to perform tasks that require high visual acuity such as recognizing faces or reading, even if peripheral vision is left relatively intact. *Image NIH open access.*

Retinitis pigmentosa is an inherited disease for which there is currently no treatment. It begins with the loss of rod photoreceptors in the peripheral visual field, followed by the loss of cone photoreceptors. The patients experience tunnel vision as the disease progress (Figure 1.5). In the later stages of disease, patients often have only a very faint remnant of vision at the very center of their visual field, which can eventually disappear as well. Visual acuity of the healthy retina is discussed in Chapter 1.8.

1.5 Subretinal photovoltaic prosthesis

This photovoltaic implant consists of tiled micro-arrays of hexagonal photodiode pixels, and is implanted into the subretinal space with the photodiodes adjacent to the degenerated photoreceptor layer. Several different photodiode devices were tested before settling on the optimal configuration. All of them were designed and fabricated at Stanford University in collaboration with Pixium Vision. Photovoltaic arrays were manufactured on silicon-on-insulator wafers using a six-mask lithographic process. Devices were produced with either 1, 2, or 3 diodes in series. Those with more diodes can produce more current at the expense of increased illumination. Pixel sizes were either 70 μm or 140μm, separated by 5μm trenches (Figure 1.7a). The larger pixels afforded greater efficiency at the expense of decreased spatial resolution. Smaller pixels allow higher resolution, at the trade-off of

higher stimulation thresholds, because the additional circuitry required for the diodes leaves a smaller active light-catching area (Figure 1.7c). To produce anodic-first pulses of electric current, the n-doped and p-doped regions in the diodes were reversed in more recent generations of the devices. A resistance between the active and return electrodes helps discharging them between the light pulses (Figure 1.7c).

Some iterations of the devices had trenches carved between the individual pixels, which allowed for better perfusion of nutrients into the retina, extending the useful recording duration for those datasets. Some devices had connected, local returns for the photodiode electrodes, and some of them had distant global returns.
Goggles worn by the patient deliver pulsed NIR light (880-915nm) to the photodiodes through the eye, from images that have been collected by a forward-facing video camera and processed by a device worn by the patient. The use of infrared light as a power source for electrical stimulation has several benefits when compared to other retinal implants which use a battery as a power source for the stimulating electrodes; it avoids the need for intraocular cables, and also preserves the use of natural eye movements to determine which cells are stimulated, rather than relying on eye-tracking technology such as the ARGUS II epiretinal prosthesis (Second Sight Inc., USA).

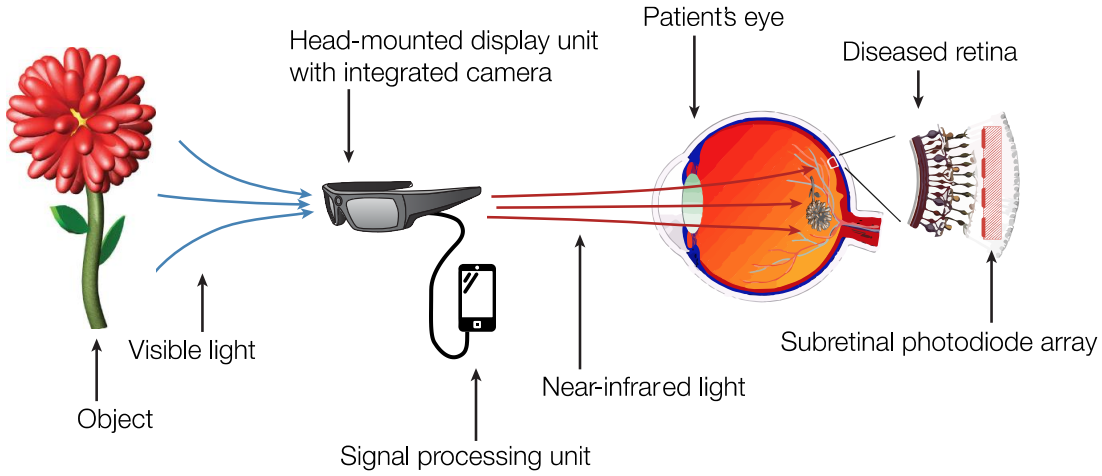

Figure 1.6: Concept of a photovoltaic retinal prosthesis. A head-mounted camera captures visual scenes, which are processed by a mobile signal-processing unit. High-power near infrared light relays visual information to a photovoltaic subretinal implant through the natural optics of the eye.

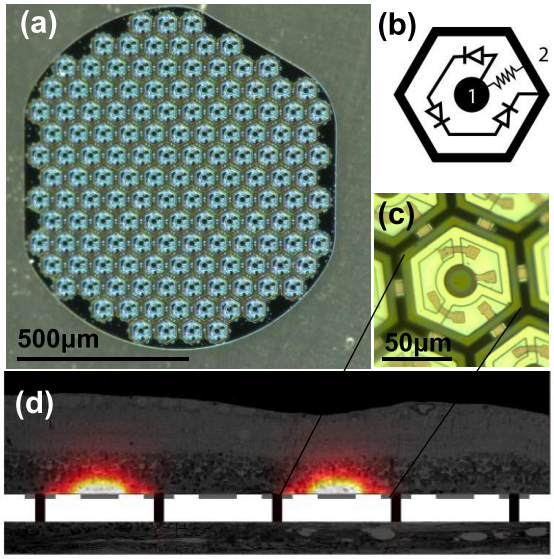

Figure 1.7 Photovoltaic array. a) Photograph of photovoltaic array with small 70μm pixels. b) Each pixel on the array consists of 2 or 3 photodiodes in series connected to an active electrode in the center (1) and a local return electrode surrounding each pixel (2). c) Close-up photograph of individual 70μm pixel. d) Simulation of the spread of electrical signal from implanted photodiodes, stimulating cells in the inner nuclear layer (INL).

With each pulse of NIR light incident on the photodiode pixels, a biphasic, charge-balanced current is produced. The pulse is either anodal or cathodal depending on the diode configuration. The first generation of devices produced cathodal-first pulses, which were not as efficient as the later anodal-first devices, both discussed in Chapter 3.

The current is produced by the photovoltaic subretinal stimulation is strong enough to reach the bipolar cell layer of the retina before returning to the electrodes, eliciting action potentials in the bipolar cells without directly eliciting action potentials in the farther ganglion cell layer (5). The layer of retina containing the bipolar cells also contains amacrine cells and horizontal cells, and is referred to as the inner nuclear layer (INL). The selective activation of the bipolar cell layer is a crucial feature of subretinal stimulation, which takes advantage of the existing hierarchy of the retina, preserving the signal integration in the ganglion cell layer, a distinct advantage compared to epiretinal stimulation which directly stimulates the ganglion cell layer (see Chapter 1.6). In this dissertation, the nomenclature pON and pOFF will be used to describe the response of cells to the onset of photovoltaic stimulation (pON) and the offset of photovoltaic stimulation (pOFF), and similarly the visible light responses are sometimes referred to as vON and vOFF (instead of simply ON and OFF) in order to more clearly distinguish them from the prosthesis-mediated stimulation.

We seek to understand the degree to which this retinal prosthesis can deliver functional vision to a patient. Our principal method of investigation is *in-vitro* examination of retinal response to electrical stimulation with this prosthesis. We use a multi-electrode recording array as described in Methods to examine visual acuity, contrast sensitivity, and the spatio-temporal response properties of individual ganglion cells.

1.6 Alternative approaches towards restoration of vision

In epiretinal stimulation, the stimulating electrodes are directly adjacent to the ganglion cell layer, an orientation which does not allow for use of the existing retinal circuitry between the degraded photoreceptor layer and ganglion cell layer, consisting of bipolar cells, amacrine cells, and horizontal bipolar cells. Epiretinal stimulation also results in direct stimulation of axons, which unavoidably creates visual streaks in patients (29). Both the epiretinal and subretinal implants tested in clinical trials enabled rather low acuity, which varied greatly among the patients. The majority of patients could not read, and among the few who could, the visual acuity was mostly below 20/1200, except for a single patient who was reported to achieve 20/550 (13). Despite its limitations, epiretinal stimulation is currently the only clinically-approved system of vision restoration.

Another type of vision restoration lies in the promise of optogenetics, which introduces light-sensitive ion channels of the opsin family into neural cells (67). This is accomplished via transfection of neural cells by a viral vector which causes the infected cells to express these light-sensitive ion channels. A very high intensity of light is required to activate the neurons, which is a limiting factor in its clinical viability, as well as the fact that the introduction of any gene-modifying viral vectors are subject to intense regulatory scrutiny.

Stem cell therapy approaches of vision restoration seek to convert embryotic stem cells into new photoreceptors after introducing them into the subretinal space. This approach has been shown to restore light sensitivity in blind mice (54), but still faces legal and practical hurdles before human use.

1.7 Optical safety considerations

NIR light (880-905 nm) used for stimulation is absorbed primarily by pigmented tissues such as the retinal pigment epithelium, with a practically negligible absorption coefficient (<0.06 cm^{-1}) in transparent ocular layers such as the cornea, lens, and neural retina. According to ocular safety standards (16), the maximum permissible radiant power (MPΦ) in J/cm^2 which may be chronically delivered to the retina is $MP\Phi = 6.93\times10^{-5}C_TC_EP^{-1}$, where $C_T=10^{0.002(\lambda-700)}$ in the 700-1050 nm range, with C_T=2.5 at □=905 nm. C_E depends on the angular spread of the incident beam and for

retinal spot sizes greater than 1.7 mm in diameter is 29.3 W/mm^2. P is the pupil factor which models pupil constriction or dilation, and is exactly 1 for infrared wavelengths in the absence of dilating drugs. For the 905 nm wavelength used in this study the average irradiance limit is 9.5 mW/mm^2. For single-pulse exposure, the peak-irradiance limit in the 0.05 – 70 ms duration range is described by the equation $MP\Phi = 6.93*10^{-4}C_TC_Et^{-0.25}$, where *t* is in seconds. At 905 nm, $MP\Phi = 285 \cdot t^{-0.25}$, where t is in ms and the result is in mW/mm^2.

The maximum irradiance permissible for our most commonly used stimulus of 4 ms pulses, is 202 mW/mm^2 (16), well above our typical maximum of 10mW/mm^2.

1.8 Spatial resolution of healthy retina

Visual acuity is one of the most important measurement of the performance of a retinal prosthesis, or vision in general, because it dictates the minimum resolvable angle between two objects. This ability to resolve fine detail determines many crucial aspects of visual life, such as how large words must be to read, or how close a face must be to identify its owner or determine its expression. The Snellen visual acuity chart (Figure 1.8a) is a commonly-used target recognition task that determines how many minutes of arc must be subtended by each part of the displayed letter, in order to be identified by the patient. Since rats cannot read, we used other methods to

determine the visual acuity, both *in-vivo* and *in-vitro*, described in the following sections.

The upper limit of visual acuity for any particular vision system will be limited by diffraction. A point spread function describes the distribution of light that falls on the retina from a single point of light due to diffraction, and Rayleigh's criteria states that the minimum resolvable angle between two points of light occurs when the peak of one of the sources' point spread function lies at the trough of the other (Figure 1.8b). Another way of describing the pixel size or (photoreceptor, for normal vision) needed to resolve a particular image is the following: to resolve two lines, there must be at least one single detector located *between* the lines, so that they are not perceived as one large line.

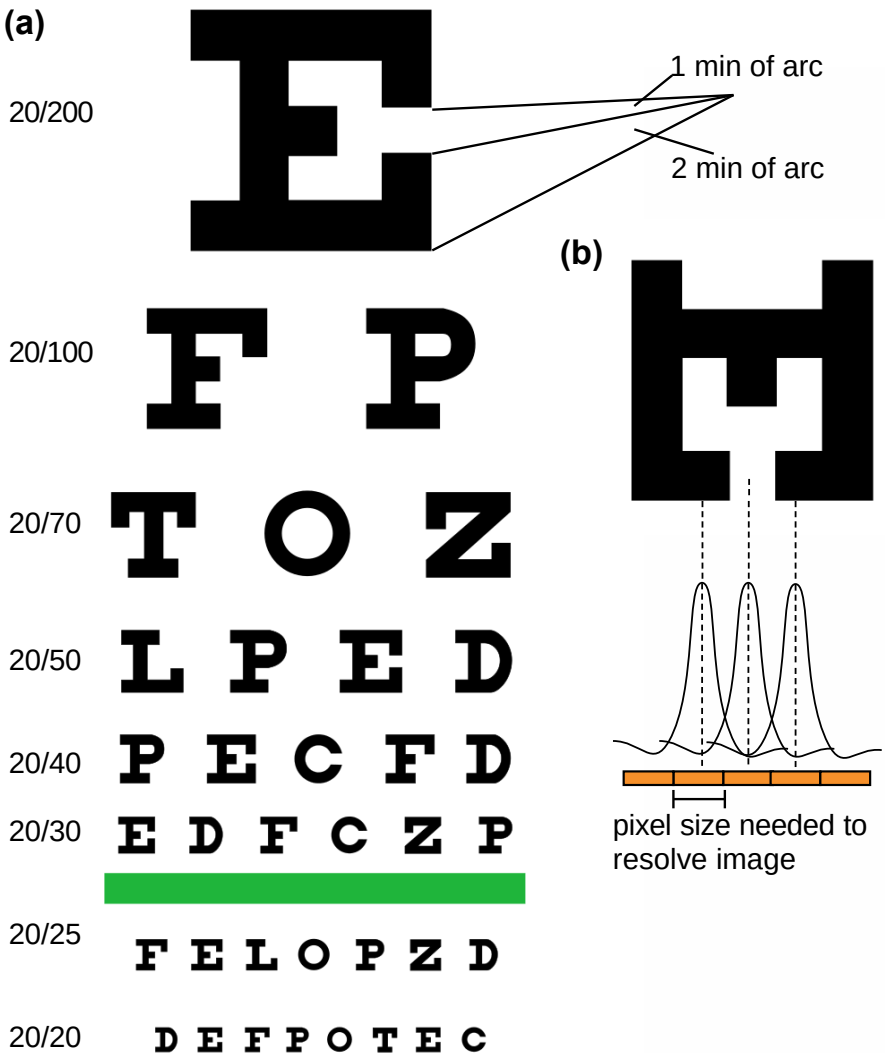

Figure 1.8 Visual acuity. a) A normally-sighted human can read the eighth line of the Snellen visual acuity chart from a distance of 20 feet, resulting in a Snellen visual acuity measurement of 20/20. Visual acuity is represented here in the units of 20/x, where x represents how many feet away from the chart a normally-sighted (20/20) human would be able to resolve that same line. b) The maximum pixel size capable of resolving this example image is dictated in part by Rayleigh's criteria, which states that for two barely-resolvable points, the peak of one's point spread function lies at the trough of the other. Furthermore, if two lines are to be resolved, a detector array needs to be fine enough to detect a gap in between the two lines.

If the lens of the eye displays a properly-focused image onto the retina, then the only other ceiling on resolution is the spacing of the individual detectors, such as

photoreceptors in the healthy retina, or individual photodiode pixels in prosthesis-mediated vision.

One of the widely-used measures of visual function is visual acuity, which quantifies spatial resolution. In the United States, the most common way to describe visual acuity is in units of 20/x which compares a patient's ability to discriminate to that of a normally-sighted human. 20/20 is considered to be normal visual acuity for a healthy human, and corresponds to the ability to resolve a visual angle of 1 minute of arc, or 2 lines that are 1.75 mm apart at a distance of 20 feet. This range of visual field corresponds to 5 micrometers on the retina. To have a visual acuity of 20/x means that the subject would be able to resolve the same stimulus at 20 feet, as a normal human would be able to resolve at x feet. So in 20/40 vision, the subject has half the normal visual acuity, and they would be able to resolve the same stimulus at 20 feet as a normal human would be able to resolve at 40 feet. People with a visual acuity of lower than 20/200 are considered legally blind in the United States, whereas the World Health Organization sets that threshold at 20/400. In countries that use metric units the Snellen visual acuity is represented as 6/x where the numerator corresponds to 6 meters.

The visual precepts elicited by electrical stimulation are inherently quite different from that of natural vision, and therefore the use of visual acuity as a measure of prosthesis performance is therefore not a complete picture of the patients'

experiences. However it is still a very useful measure of prosthesis performance because it will accurately describe, for instance, how large letters and words must be for a patient to be able to read them, or how far apart two people's faces must be to resolve them as separate objects. In the following chapters, we will measure visual acuity performance in a number of ways that relate to this standard.

Chapter 2: Methods

2.1 Multi-electrode recording system

Santa Cruz Institute for Particle Physics (SCIPP) became involved with neural recording and stimulation research when it became apparent that some of the components of the particle physics detector technology would be useful in the construction of a high-density multi-electrode recording array (MEA). One of the largest challenges in the design of such a high-density array is the puzzle of arranging hundreds of individual leads for the electrodes in such a way that they do not interfere with each other. Several different iterations of the MEA were produced, including the version that we use for most of this research, which consists of 512 electrodes, the ability to both stimulate and record from individual electrodes, and a sampling frequency of 20,000Hz. The 512 individual electrodes are spaced 60 μm apart in a hexagonal grid, and cover an area of 1.7 mm^2. On-board amplifiers allow us to adjust the gain of the electrodes, which is a crucial feature that allows for better preservation of the electrical artifact shapes, avoiding over-saturation and allowing us to remove the large electrical artifacts from the data. A recording chamber approximately 2cm wide and 2 cm deep holds the retina and the perfusion fluid (Figure 2.1).

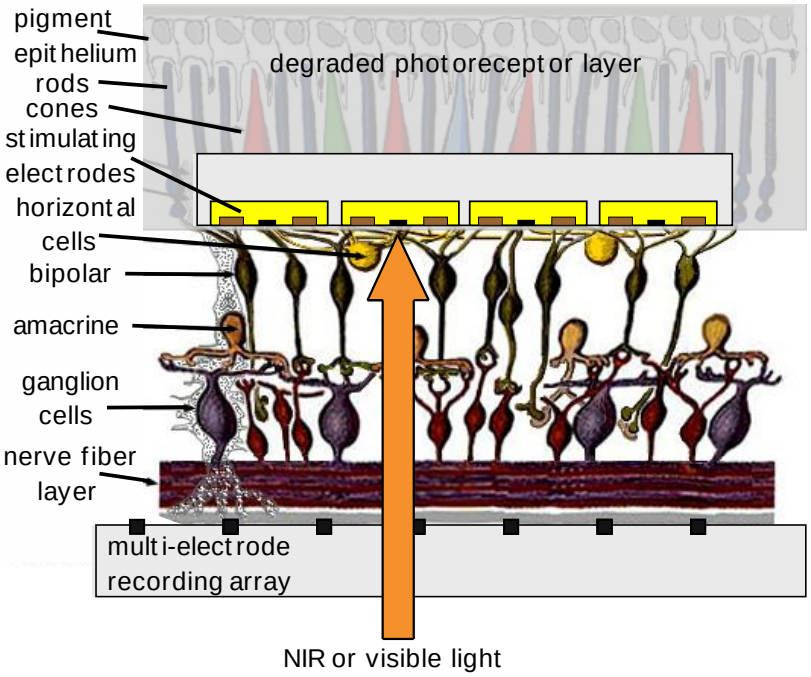

Figure 2.1 Photovoltaic array and experimental setup. Schematic representation of a degenerate rat retina sandwiched between a transparent multielectrode array (MEA) which records from the ganglion cell layer (GCL) and the photovoltaic array (PVA). Visible light stimulates the photoreceptors (PR), while much brighter pulsed NIR (880–915 nm) illumination generates biphasic pulses of current in the photovoltaic pixels, stimulating cells in the inner nuclear layer (INL). *Background image of retina: Copyright 2016 Webvision.*

The voltages from the 512 electrodes are read out by eight “stimchips”. Each of the stimchips has 64 channels of 150-pF capacitors which ac-couple the electrode signal to the corresponding channel (35). Each of those stimchip channels is also equipped with a current generator for electroplating each electrode with platinum, which reduces the impedance on each electrode, and consequently reduces the recorded electrical noise. This is achieved using a solution of chloroplatinic acid and selectively delivering current to one chip at a time. Visual monitoring of the

electrodes is used to determine that they are accumulating a layer of platinum and increasing in size, and additionally, the rms input noise is monitored before and after the electroplating to verify its decrease. Each stimchip channel is therefore capable of stimulating cells as well, though this functionality was not used in our experiments. However, the related ability to decouple the signal from the electrodes was used, to blank out the stimulation artifacts delivered by the prosthesis and avoid over-saturation of the preamplifiers on the stimchip. Each stimchip has 64 channels of differential preamplification, output amplification, and bandpass filtering. The passband, is typically set to 80-2000Hz, the overall gain is typically 1500, and the equivalent rms input noise is about 5 μV.

The array is transparent and we project either NIR or visible light through the recording electrodes onto the retinal tissue or underlying prosthesis, after which we record action potentials from RGCs on the recording electrodes. The voltages from the 512 electrodes are recorded onto an external hard drive connected to a PC with specially designed Labview software. Concurrently, the data is streamed to a Macintosh desktop computer sitting alongside, running custom software called Vision, which was developed at SCIPP.

2.2 Optics and equipment

The design of our experiments necessitates the use of visible light to stimulate the retina naturally, and near-infrared (NIR) light to activate the photodiode implants and produce electrical stimulation. To evaluate the prosthesis-mediated vision, we used a NIR projection system consisting of a polarization-scrambled array of 880 nm laser diodes coupled into a 400µm multimode fiber (Dilas M1F4S22-880.3-30C-SS2.1). The laser beam is collimated at the output of the fiber and a 2° divergence microlens array diffuser improves the homogeneity of the beam before it is projected onto the implant via the camera port of an inverted microscope (Olympus IX-71, 5x objective). The visible light was produced with a yellow LED which joined the same optical path before entering the microscope. Both light sources were modulated with a National Instruments USB-6353 data acquisition card and custom software. Both light sources also pass through the same LCD screen before entering the microscope, allowing for specific images to be focused onto the photoreceptor layer of the retina.

2.3 Dissections and experimental procedure

Retinal tissue is explanted from an anaesthetized (isoflourine) and euthanized (390 mg/ml pentobarbital sodium, 50 mg/ml phenytoin sodium) rat, the retinal-pigmented epithelium is removed, and the isolated retinal piece is placed ganglion-cell side down in the MEA recording chamber, where it is constantly perfused with

oxygenated Ames (Sigma) medium to supply metabolic needs to the tissue. The temperature of the medium was maintained at the relatively-cool temperature of 29.4°C, so that the metabolic needs of the retina would not be too great. For wild-type control experiments with visible light, there was no photovoltaic implant on top of the retina, and for the prosthesis experiments, an implant was placed carefully on top of the retina before the following step. The tissue is carefully pressed down with 100 μm silicon mesh so that the retinal ganglion cells make good contact with the recording electrodes, but not with so much pressure that the retina was damaged. Failing to obtain this delicate balance of pressure in this step accounted for the majority of the failed experiments. Once the tissue is secured on the MEA, a variety of visual and electrical stimulus is delivered to the piece. Recordings from healthy retina can provide significant RGC responses for up to 10 hours after the piece is mounted.

2.4 Neuron finding

2.4.1 Spike sorting

Voltage traces from 512 electrodes with 20,000Hz sampling frequency provide a large amount of data, during the 3-6 hours of recording per experiment. Each electrode often picks up spikes from 5-10 different RGCs. Action potentials from individual RGCs are detected when the voltage on any trace surpasses a defined threshold. Through the use of principal component analysis (PCA), spikes are

clustered in a multi-dimensional space (Figure 2.2a) that uses attributes of the action potential shapes to assign them to individual RGCs. An additional step of neuron cleaning ensures that there are no 2 spikes assigned to a single neuron within the refractory period of 1 ms, during which it is impossible for a single RGC to fire twice.

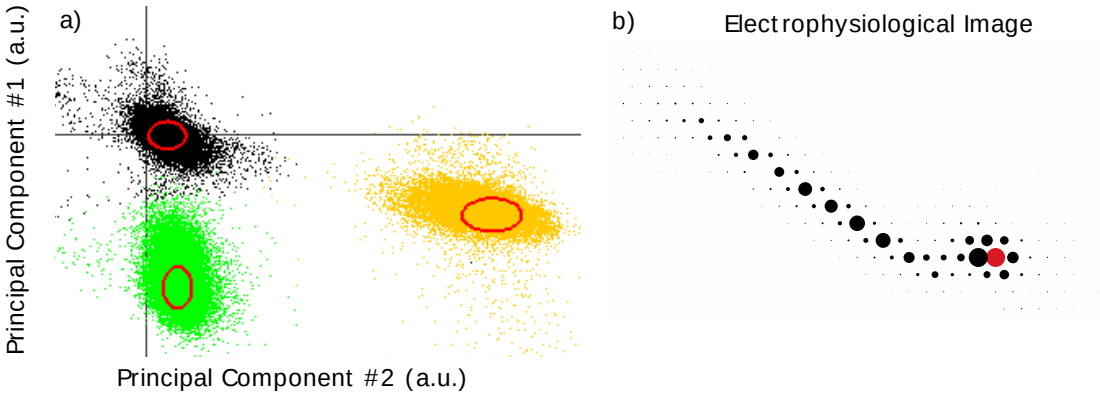

Figure 2.2 Neuron identification. a) Principal component analysis is used to plot each action potential in several dimensions (2 shown here), each representing different quantified properties of the action potential shape. Clustering assigns individual spikes to RGCs, sorting through the multitude of overlapping electrical signals. b) The electrophysiological image (EI) of each cell is calculated by correlating voltage signals recorded over the array with the sorted spike trains. The size of each dot in this image depicts the average amplitude of the voltage recorded on each electrode following an action potential for this particular RGC, whose soma is located near the cluster of electrodes containing the red electrode, representing the maximum voltage deflection. The axon is visible trailing off to the left.

For each neuron, we calculated the electrophysiological image (EI) of the neuron, i.e. the average voltage waveform recorded on the whole multielectrode array when the neuron produced an action potential (50), (Figure 2.2, b). We discarded neurons exhibiting abnormal EIs from the analysis, as well as neurons for which violations of the refractory period occurred within the action potential train. A typical EI is a short movie showing the spiking cell body followed by the propagation of the spike down

the cell's axon. Abnormal EIs consist of 1) backwards-propagating signals down the axon *towards* the soma, caused by signal reflection at the severed edge of an axon, 2) cell bodies lacking an axon, and 3) voltage fluctuations inconsistent with neural origin, such as electrical artifact remnants from the photodiode pulse, visible across the entire electrode array (see the following section on artifact removal). The similarity between two EIs can be examined by calculating their inner product. We removed neurons with the same EI from the analysis, as they correspond to redundant detections of a single neuron over multiple electrodes, and only the putative neuron with the largest action potential count was kept. This is done automatically in the Vision software by setting bounds on the minimum reduced chi-squared of the EI inner product, as well as placing maximum bounds on the separation between a neuron and its supposed duplicate. EIs were also useful in tracking cells from dataset to dataset, necessary when comparing results of different stimuli, This was done using custom MATLAB scripts operating under similar algorithms as the Vision software. It was not always possible to track cells between datasets, and visual confirmation of each individual EIs was necessary to confirm that the cell had been successfully tracked. The neuron selection process is described in the section on white noise stimulus (2.5.1) and in the literature (44).

2.4.2 Artifact removal

For datasets in which the photovoltaic stimulation was used, a large electrical artifact is produced by this stimulation, often 10-20 times larger in amplitude than the action

potentials we are trying to record. To remove them, we employ a MATLAB script that subtracts these artifacts from the raw traces of each electrode. First, the initial 8.25 ms of data after each pulse is discarded and replaced with noise, because the artifact shape is too unpredictable in that region (Figure 2.3a). Then, the remaining portion of each individual artifact, on each of the 512 electrodes, is fitted to this double-Gaussian:

$$f(x) = ae^{((x-c1)/d1)^2} - be^{((x-c2)/d2)^2},$$

in a procedure that takes approximately 10 hours for a 5000 second dataset on a 3.2GHz 8Gb Macintosh desktop computer, resulting in about 51,000,000 individual fits. Each individual fit is subtracted from the raw trace of each electrode's voltage, resulting in an artifact-removed version of the data, which retains most of the original action potentials, except for those that occurred in the 8.25 ms following the start of each pulse. As a consequence, all possible direct stimulation of the RGCs (latency ≤ 1ms) was ignored in our analysis, (8).

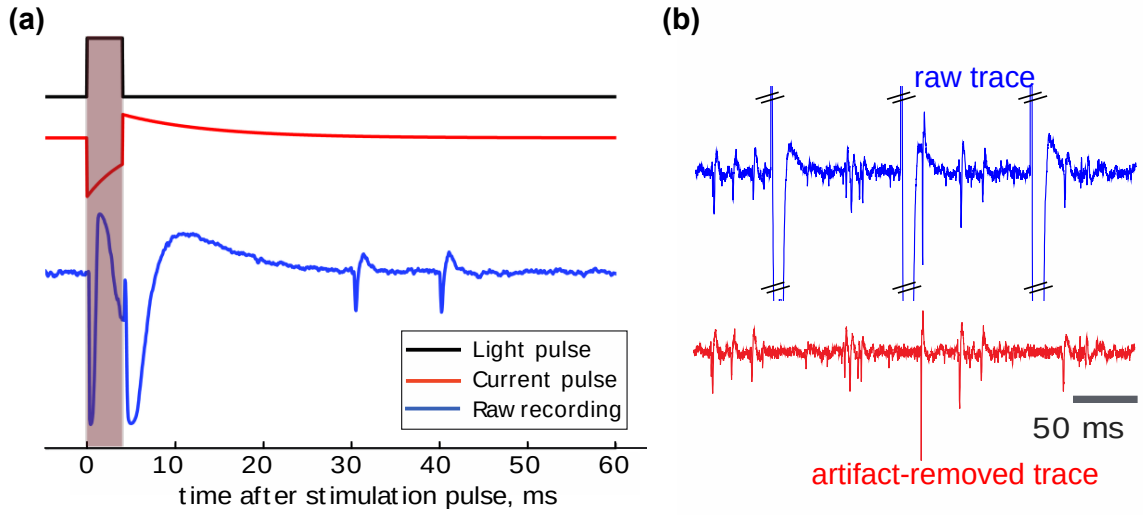

Figure 2.3 Artifact removal (a) Single pulse of light with the resulting artifact and elicited spikes. (b) Sample trace from one electrode as a result of 20Hz photovoltaic stimulation showing the raw trace in blue and the artifact-removed trace in red.

Previously, the artifact-removal algorithm utilized an averaging technique, which assumed that for each of the electrodes the artifact remained unchanged throughout the recording. This limited our ability to use stimuli that had a lot of variation, such as a flickering white noise stimulus described in Chapter 2.5. With the individual Gaussian fitting for each artifact, however, we are able to use rapidly changing, high-frequency stimuli. After the artifact removal we are left with raw voltage traces containing action potentials, which can be processed in the same way as the visible light data which lacks electrical artifacts, described in Section 2.4.1.

2.5 Stimulus

Several different types of visual and electric stimuli were used to characterize the retina's normal visual responses in addition to its response to photovoltaic stimulation. They are described here and the results obtained from these measurements are outlined in the following chapters.

2.5.1 Thresholds measurements

One of the important quantities to determine for any type of retinal prosthesis is the threshold for stimulation. The amount of light delivered to the retina must be below ocular safety limits but high enough to reliably elicit photovoltaic stimulation of the retina. Electrical current is produced from the photodiodes when they are in the path of 880-915 nm NIR laser light. To determine the threshold for response, full-field laser light was projected onto the photodiodes on top of explanted retina at 2Hz, with pulse widths varying from 1 to 10 ms, and irradiance varying from 1 to 15 mW/mm^2. Threshold for response is categorized as >0.5 spikes per pulse of laser light, at 2Hz. It is observed that by lengthening the pulse width while maintaining the same level of irradiance, the threshold for irradiance decreases until the pulse width reaches 4 ms. Beyond that, increasing the pulse width has no effect on reducing the irradiance threshold. Therefore, 4 ms was chosen as the optimal pulse width for all the remaining stimuli involving electrical stimulation. With 4 ms pulses, 2- and 3-diode devices showed greater response at all irradiances, and had corresponding

thresholds of 5 and 10 mW/mm^2, respectively. The thresholds results for different configurations of the device are discussed in Chapter 3.1.

2.5.2 Contrast sensitivity

The number of gray levels that a patient can perceive with a retinal prosthesis is an important measure of how much useful information the device can deliver, because it dictates how much more gray one of two adjacent areas must be in order to be recognized as different, as well as how much an area must change its gray level over *time* to be recognized as having changed. The two concepts are closely related because natural eye movements cause different parts of a visual scene to quickly fall upon different parts of the retina. Other, recent subretinal implants (4) failed to deliver more than 2 or, at most, 3 discernible gray levels. To measure contrast sensitivity we used a full-field NIR stimulus which changed its overall brightness at 2Hz, while the carrying frequency of the laser was maintained at 20Hz (Figure 3.1.2) Each alternate image was a full-field maximum irradiance level (10 mW/mm^2), while the other images were full-field images of lower irradiance levels. We sought to determine which contrast levels would be sufficient to elicit stimulation from the retina, for both increases and decreases in light level. A similar stimulus protocol was delivered for control experiments with visible light. For electrical stimulation, the retina responded to both the increase and decrease in illumination by NIR light, although the thresholds for response were much larger than in visible light stimulation of healthy retina, requiring on average 65% increase or 80% decrease in

illumination to reliably elicit stimulation, as compared to 7% increase or 3% decrease with visible light. This discrepancy necessitates additional pre-processing steps to enhance the contrast of the images being displayed to the patient. The results from this stimulus are discussed in Chapter 3.1.

2.5.3 Contrast-reversing gratings

Perhaps the most important measure of a visual prosthesis' performance is the degree to which visual acuity can be restored in a patient. The Snellen visual acuity of a healthy person is 20/20, which corresponds to the ability to perceive 30 cycles per degree, or 30 pairs of black/white gratings in one degree of the visual field. To examine this subretinal implant's ability to resolve detailed images, we used a stimulus of black and white contrast-reversing gratings, whose color alternated sinusoidally in space between black and white (Figure 3.2.3), at different temporal and spatial frequencies. This is a commonly-used stimulus for measuring visual acuity in infants and animals (25), because it is possible to record visually-evoked potentials (VEP) from the back of visual cortex at the back of the head, even with surface electrodes. Those VEPs disappear as soon as the retina stops being able to discriminate between adjacent bars. This same stimulus was used in both the visible light stimulation and the prosthetic stimulation, *in-vitro* and *in-vivo*, and the results are discussed in Chapter 3.2.

2.5.4 White noise stimulus

The white noise stimulus is a robust and effective way of simultaneously characterizing the spatial and temporal response properties of a large group of RGCs. The beauty of a randomized stimulus is that the average spike-producing stimulus for any given neuron can be reconstructed to produce an idea of what the most favorable stimulus is for that neuron (10). Therefore it is possible to obtain the estimate of the linear filter represented by the RGC and all the retinal circuitry feeding into it. Such a stimulus is capable of identifying several distinct ganglion cell types. In our case, the spatiotemporal monochromatic white noise stimulus consisted of 100 x 60 square pixels, each one 70 μm per side and randomly assigned as black or white, and changing to a new image every 33.33 ms. If .5 represents the mean background gray level, the relative light intensity of each pixel was 0.5 ± 0.48. The corresponding contrast, $(I_{max} - I_{min})/(I_{max} + I_{min})$, was therefore 96%, where I_{max} and I_{min} are the maximum and minimum intensities, respectively. The light used was of wavelength 591 nm and the intensity of the background gray level corresponds to roughly 22,000 photons/μm^2/sec.

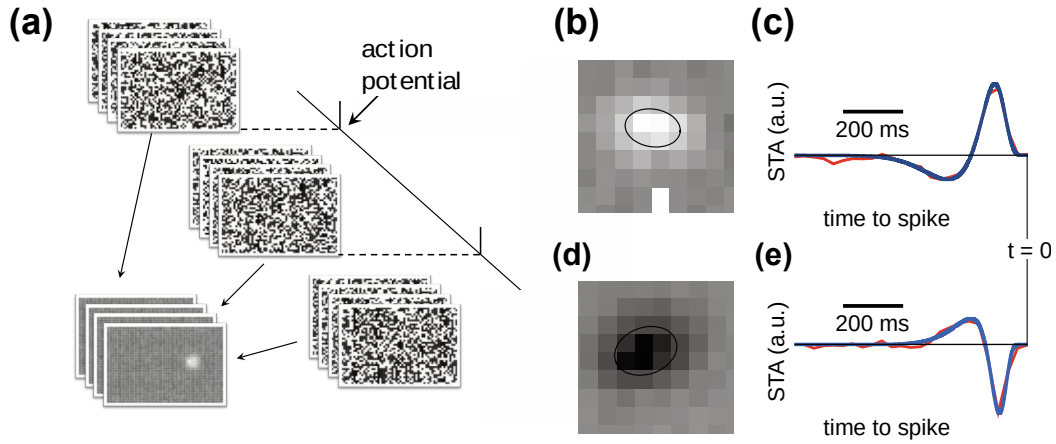

Figure 2.4 Spike Triggered Average (STA) response to binary white noise stimulus. a) The STA is the frame-by-frame average of the short spatio-temporal white noise movie that precedes each action potential of an RGC. The spatial sensitivity profile of the RGC (receptive field) corresponds to the STA regions with significant deviation from the average gray level. For an ON (b) and OFF (d) rat retinal ganglion cell, the STA frame corresponding to the largest deviation from gray level within the receptive field is shown, with the pixels' greyscale normalized in relation to the whitest and darkest pixel in the STA. The spatial extent of the receptive field is quantified by fitting a 2-dimensional Gaussian to this STA frame. An elliptical 1-σ contour of the fit is overlaid on top of the receptive field. The pixels located within these receptive fields are used to construct the visual time courses (c, d), which show the average STA intensity of the pixels located within the receptive fields for each STA frame leading up to the spike. Overlaid over each time course is a fitted difference of low pass filters. The response latency is estimated as the time to the first zero crossing of the fitted function.

To calculate the visual receptive fields, we computed the spike-triggered average (STA) RGC response to the white noise stimulus projected on the retina. We did so by averaging, over all spikes generated by the neuron, the sequence of stimulus frames preceding each spike (Figure 2.4a), (10). The receptive field shape and location were based on the STA frame which differed most significantly from the mean (gray) background level. We fit this significant frame with a two-dimensional Gaussian, where the RF diameter is defined as the mean of the minor and major axes of the ellipse comprising the 1 SD contour of the fitted Gaussian (Figure 2.4b,d). The

time course of each neuron is an average of the STA intensity of pixels within the cell's receptive field, plotted as a function of time preceding spike.

In the linear-nonlinear (LNL) model of the retina, an RGC responds non-linearly to visual input that has gone through a linear spatio-temporal filter. This allows RGCs to change their response to stimuli that otherwise would predict a steady output in a strictly linear model. For example, if the all of the photoreceptors on one half of a RGC's receptive field were illuminated, and then the illumination was reversed, a strictly linear model would predict no change in the RGCs output, but experiments have shown otherwise (8, 63). Additionally, a linear model fails to account for spike threshold and maximum possible spike rate, dictated by the refractory period of each neuron. Part of the beauty of using a white noise stimulus is that, by providing a linear input as a stimulus and convoluting the time course with the full field step in illumination, we can obtain the predicted response of the cell to such a step, and thereby obtain the time filters used by these non-linear subunits of the retina (Figure 2.4c,e), (10).

Each stimulus vector s(t) is a randomly-generated sequence of white noise images with the number of frames equaling the neuron's memory: in our case about 4 frames at 30Hz. The expected response of a ganglion cell R(s), in terms of spikes per unit time immediately following each stimulus (t), can be predicted from this stimulus vector alone, and has a nonlinear part N is addition to the linear spatio-temporal

weighting of the stimulus vector s:

$$R(s) = N(w \cdot s).$$

It can be shown that the linear weighting on this stimulus vector, w, is directly proportional to the STA (10), allowing us to estimate the nonlinear component of the expected response. In this way, the white noise provides a simple way to predict the response of a cell despite arbitrarily complex processing that might occur within the retinal layers.

It is possible to discern certain several different ganglion cell types using the white noise stimulus. The sign of the first peak preceding the spike in the time course determines if the RGC will increase its spike rate in response to the ON- or OFF-set of light (10). Some of the distinct classes of ganglion cells we can detect in this analysis include ON-center, which respond to an increase in illumination; OFF-center, which respond to a decrease in illumination; transient cells, which have a biphasic STA; and sustained cells, which have a monophasic STA. For each of these categories, the STA will show an average of the stimulus which preceded each spike, which is a rough representation of that neuron's preferred stimulus.

Other defining characteristics of specific RGC types include their response latency (brisk or sluggish) and *transiency*, which can be transient (biphasic time course) or sustained (monophasic time course). The response latency can be defined either by the time before spike of the first peak of the time course, or the first zero crossing.

Each of the approximately 20 individual RGC types forms a mosaic of receptive fields (Figure 2.5), (18; 13; 51).

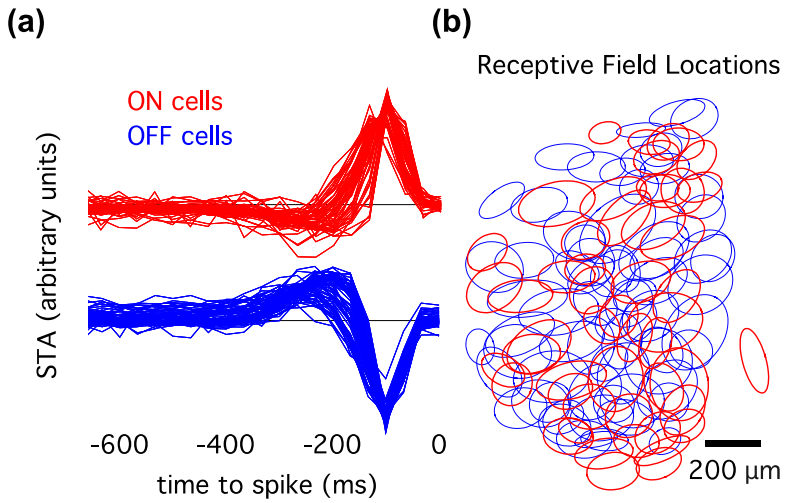

2.5 Receptive fields from distinct RGC classes form mosaics over the visual field. a) The time courses for ON (red) and OFF (blue) RGCs show distinct responses to visual white noise stimulus with opposite response polarities. b) The receptive fields from those same cells, shown in corresponding color, each form a mosaic over the same area of the visual field.

2.5.5 Sparse white noise stimulus

Our first attempts at characterizing the electric receptive fields (eRFs) with the photovoltaic implants utilized a sparse white noise stimulus. Much like the white noise stimulus described above, we sought to understand the spatio-temporal response properties of the retina in response to photovoltaic activation. But we were hindered by the fact that our artifact-removal procedure (see Chapter 2.4.2) relied on an averaging process to remove the average electrical artifact on each electrode,

before we adapted our system in order to allow for evolving artifact shapes and hence a more robust, true white noise stimulus. So in the meantime we activated one photodiode pixel at a time, in a semi-random order, so that we could eventually obtain information about which photodiode pixels were able to stimulate which RGCs, building a picture of the electric receptive fields for all the responsive RGCs. We selectively activated one pixel at a time with 70um diameter NIR laser light. RGC response was categorized based on the number of spikes per laser pulse, which occurred at 2Hz for this stimulus, with the threshold for response defined as >0.5 spikes per pulse. Some RGCs responded only to the activation of one particular pixel, and others responded to a collection of nearby pixels. For each RGC, we determined the electric receptive field, an elliptical area defined by taking the 1-sigma contour of a 2-dimensional Gaussian of the number of spikes elicited by each pixel, centered on that neuron. The results are discussed in Chapter 3.2.

This stimulus was limited to single-pixel activation because the artifact-removal algorithm we were using at the time was unable to remove artifact shapes that evolved over time; it employed an averaging method which demanded consistent artifact shapes throughout each recording. Later, we developed an improved version of the artifact-removal, which relied on individual fitting for each artifact pulse on each electrode, enabling us to use high-frequency, dynamic images. This ability led us to perform the stimulus detailed in the following section, which comes close to approximating a real-world dynamic visual scene.

2.5.6 High-frequency hexagonal white noise stimulus

With the development of more dynamic artifact-removal procedures we were able to run a prosthetic stimulus that closely mimics the robust visible light white noise stimulus described in Methods. Instead of a rectangular grid of black and white squares, we employed a hexagonal grid where each hexagonal pixel was aligned to illuminate one pixel on the prosthesis.

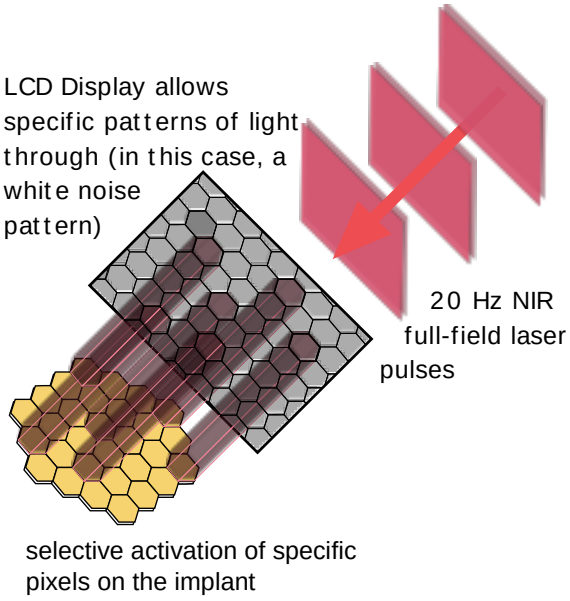

Figure 2.6 Delivery of NIR high-frequency hexagonal white noise stimulus to the prosthesis.

We chose a 20Hz stimulus for both the laser pulses and the image refresh so that we would still have a useful amount of data per second after removing stimulus artifact.

It is possible that the retina would respond to even higher image frequencies, but we were limited by the requirement that we remove 20 pulses per second of 8.25 ms each, or about 17% of the data. Yet this frequency is high enough to mimic natural visual scenes, approaching cinematographic frame rates. The results from this stimulus are discussed in Chapter 3.3.

Chapter 3: Results

3.1 Thresholds and contrast sensitivity

3.1.1 Full field thresholds

One of the important quantities for any type of retinal prosthesis is the threshold for stimulation. The amount of electrical current delivered to the retina must be below ocular safety limits but high enough to reliably elicit stimulation from the retina. Electrical current is produced from the photodiodes when they are in the path of NIR laser light. To determine the threshold for response to individual pulses, laser light was projected onto the photovoltaic array on the photoreceptor side of explanted retina at 2Hz, as described in Methods, with pulse widths varying from 1 to 10 ms, and irradiance varying from 1 to 15 mW/mm^2. The threshold for response is defined by a neuron surpassing a firing rate of 0.5 spikes per pulse of laser light, at 2Hz, or a spike for every other pulse of light. It is observed that by lengthening the pulse width while maintaining the same level of irradiance, the threshold for irradiance decreases until the pulse width reaches 4 ms (Figure 3.1.1). Beyond that, increasing the pulse width has no effect on reducing the irradiance threshold. Therefore, 4 ms was chosen

as the optimal pulse width for all the following stimuli involving electrical stimulation.

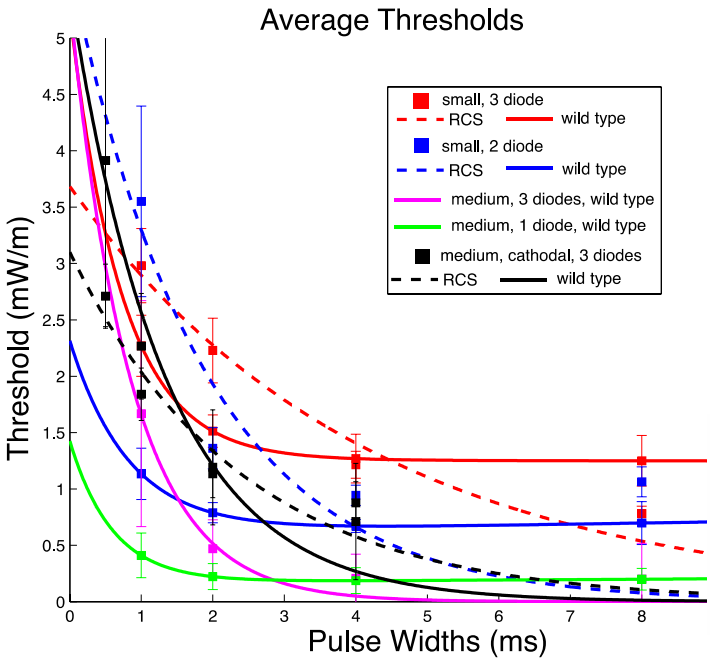

Figure 3.1.1 Strength-duration plot for wild-type and RCS rat retinas. Showing the average stimulation thresholds values and exponential fits for 140µm (medium) and 70µm (small) single, double, and triple diode devices. Stimulation threshold is defined as the irradiance in mW/mm^2 required to elicit an action potential for every other pulse of light delivered, at 2Hz. All of the curves shown are for anodic-first polarity, except those shown in black. The cathodic devices had higher thresholds compared to their anodic counterparts. The RCS degenerate retinas (dashed lines) had higher thresholds compared to their wild type counterparts (solid lines). Generally, devices with more diodes had higher thresholds, as well as devices with smaller pixels.

Devices with larger pixels had lower thresholds (Figure 3.1.1), since they had greater light-catching areas per photodiode. Since the smaller 70µm pixel devices were capable of passing the threshold for stimulation, they are the better choice because smaller pixels can allow for higher spatial resolution. Increasing the number of diodes on each photodiode pixel increases the maximum voltage that can be

delivered, at the expense of a smaller active light-catching area due to the additional circuitry required, which in turn necessitates higher light levels to achieve stimulation. Although the 70μm, 2 diode devices has higher thresholds than the 140μm, 1 diode devices, the increased density of the 70μm configuration is desirable for attaining higher spatial resolution. The irradiance required for stimulation with the smaller pixels was still well below ocular safety limits (see Chapter 1.7). Among the 70μm pixel devices, the 2 diode devices had lower thresholds than the 3 diode devices, so this design was chosen as the optimal configuration for most of the following experiments.

3.1.2 Contrast sensitivity

For a more thorough analysis of thresholds at continuous illumination levels and varying contrasts, we used a carrier waveform consisting of 20Hz, 4 ms pulses of near-infrared light. We modulated the envelope of the carrier waveform using a square wave consisting of a 0.5 second-long maximum value of 2.5 mW/mm^2 (140μm pixels) or 5mW/mm2 (70μm pixels) followed by a 0.5 second-long minimum value randomly selected between 0 and the maximum intensity (Figure 3.1.2b). We used n = 150 trials for each intensity value, in order to maintain adequate statistical power with increased noise levels due to electrical stimulation.

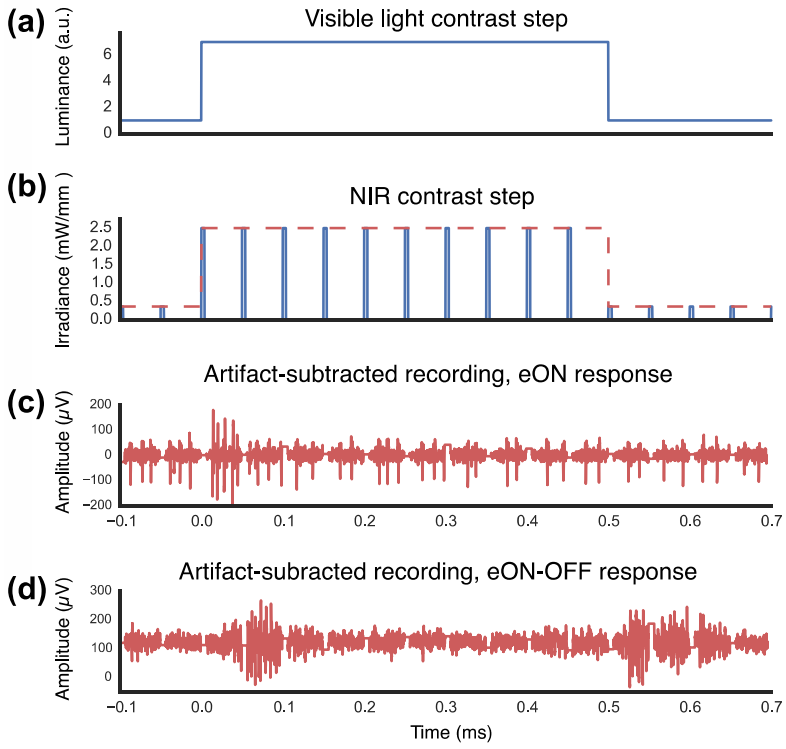

Figure 3.1.2 Contrast sensitivity stimulation protocol. a) With visible illumination, contrast steps are presented using continuous illumination. b) Prosthetic stimulation consists of contrast steps with the same envelope modulating a 20Hz train of near-infrared pulses. c), d) Voltage traces from two different electrodes. Note that the periodic "quiet" regions in these traces coincide with the removed stimulation artifacts during which information about the waveform was lost due to amplifier saturation. c) Two neurons were detected on this electrode, one of which (larger amplitude action potentials) responded transiently to the positive contrast step while the other (smaller action potentials) did not respond to stimulation. d) On this electrode, neurons transiently respond both to the positive and the negative contrast steps.

The rest of this chapter 3.1 is a modified version of our previously published work (23):

For each contrast step, we constructed peristimulus time histograms (PSTHs) by binning action potentials over 5 ms periods and averaging over 100 (visible) or 150 (prosthesis) trials. We used the Michelson definition for relative contrast (I_{post} –

I_{prev})/(I_{post} + I_{prev}), where I_{prev} is the luminance (or peak intensity for prosthetic stimulation) pre contrast step and I_{post} is the luminance post contrast step. We defined the steady-state retinal activity as the firing rate over the 300-500 ms period post-stimulus. For visible light stimulation, we compared the steady-state activity to the activity in the 50-150 ms following each contrast step. The amplitude of the response was quantified as the positive variation from steady-state activity in number of action potentials. For prosthetic stimulation, latency of the elicited action potentials was shorter (44), likely because electrical stimulation bypasses the slow phototransduction cascade. Therefore, steady-state activity was compared to the activity in the 0-100 ms following each contrast step. All neurons that did not respond to at least one value of contrast change with an average of 0.5 action potential elicited per trial were considered non-responsive and were discarded from the analysis. We included in the analysis the experimental preparations in which at least 10 RGCs underneath the implant responded to 100% contrast steps over the full-field.

For each neuron, we plotted the number of elicited action potentials vs. amplitude of the contrast step, and fitted the resulting curves with two generalized sigmoid functions, one for the OFF component of the response and the other for the ON component, such that:

$$\begin{cases} r = f(\log(-c), \tau_l, \mu_l, \sigma_l, \rho_l) \text{ if } c < 0 \\ r = 0 \text{ if c = 0} \\ r = f(\log(c), \tau_r, \mu_r, \sigma_r, \rho_r) \text{ if } c > 0 \end{cases}$$

where $f(x, \tau, \mu, \sigma, \rho) = \tau\left(1 - e^{\frac{-(x-\mu)}{\sigma}}\right)^{-\rho}$, c is the contrast, r the response of the neuron, and μ, σ, τ and ρ are fitting paramters for a generalized sigmoid function.

We defined the stimulation threshold as a 50% probability of eliciting an action potential, as estimated from the generalized sigmoid fit. We classified neurons that responded primarily to luminance increments with prosthetic stimulation as electrical ON cells (pON). The threshold for a significant response for a pON cell was defined by having the ratio of (max(ON response))/(max(ON response) + max(OFF response)) above .75, where the max(ON) response refers to the number of spikes per contrast level of the maximum positive contrast change. We classified neurons that responded primarily to luminance decrements with prosthetic stimulation as electrical OFF cells (pOFF) by using the corresponding criteria of having the ratio of (max(OFF)response)/(max(ON response) + max(OFF response)) above .75. We classified neurons that responded to both luminance increments and decrements as pON-OFF cells.

To measure contrast sensitivity of the healthy (wild-type, Long Evans, WT) rat retina, we projected full-field visible light steps of varying amplitude on the photoreceptor layer. We projected similar patterns on a photovoltaic implant pressed on the photoreceptor side of WT and degenerate (Royal College of Surgeons, RCS)

rat retina using high frequency near infrared (NIR) illumination (Methods and Figure 1). Responses to both visible light stimulation and near-infrared stimulation could be classified as ON, OFF or ON-OFF (Figure 3.1.3). We will denote visible light responses as vON (Figure 3.1.3b), vON-OFF (Figure 3.1.3c) and vOFF (Figure 3.1.3d) in the rest of the text in order to distinguish them from their prosthetic counterparts, electrical pON (Figure 3.1.3e), pON-OFF (Figure 3.1.3f) and rare, weak pOFF (Figure 3.1.3g, n=9/75 neurons for WT retina and n=2/93 neurons for RCS retina).

Responses to prosthetic stimulation exhibited shorter latencies than responses to visible light (typical latency of 0-100ms following the contrast step, as compared to latencies of 50-150ms for visible light stimulation), likely because prosthetic stimulation bypasses the slow phototransduction cascade (44). The ratio of stimulation thresholds between ON-center and OFF-RGCs was 1.24 ± 0.31, not substantially different between the two cell classes.

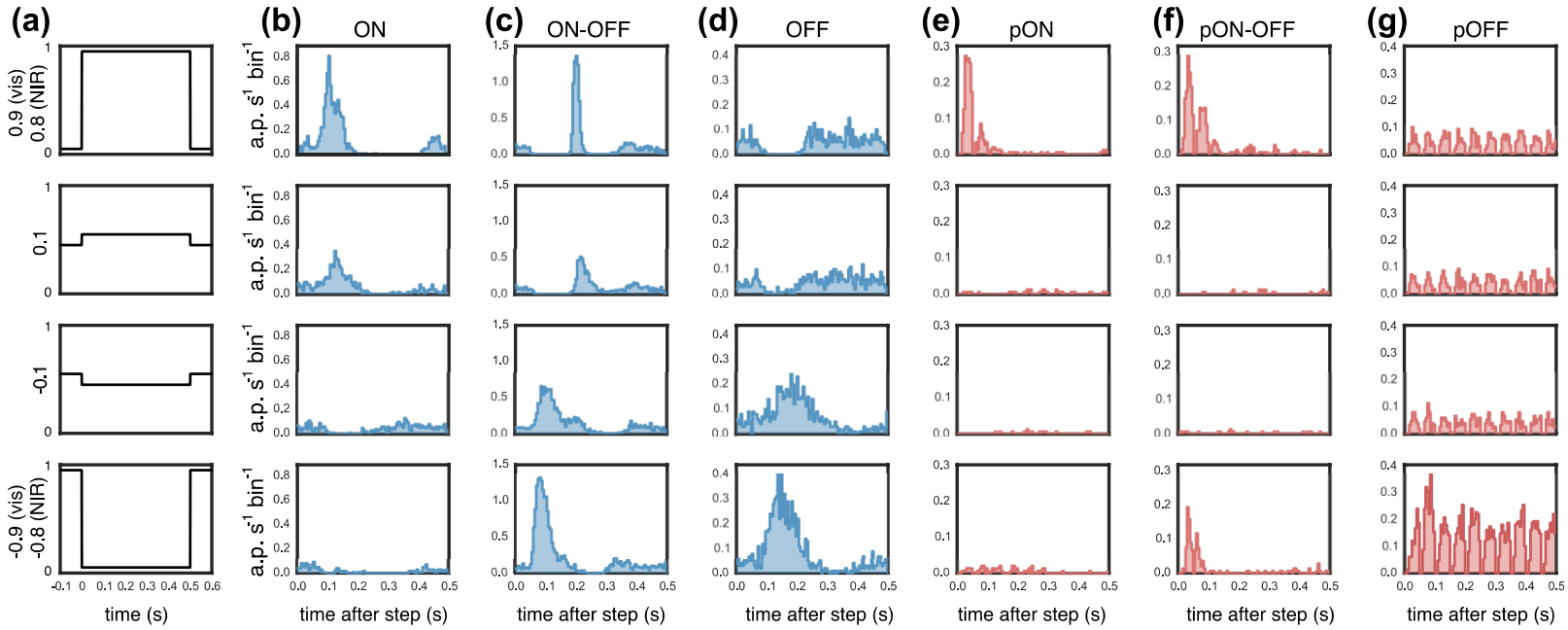

Figure 3.1.3: Single-unit responses to contrast steps. b) vON, c) vON-OFF and d) vOFF responses to a) full-field contrast steps observed with visible light in the WT retina. Neurons responded to both high and low contrast steps. Similar e) pON, f) pON-OFF and weak g) pOFF responses observed with electrical stimulation in the degenerate RCS retina. With electrical stimulation, neurons did not respond to lower contrast steps. The periodic gaps in the histograms are due to electrical stimulation artifacts, which prevent detection of action potentials during the stimulation pulses.

The proportion of pON, pOFF and pON-OFF responses varied significantly between healthy and degenerate animals as well as between RCS animals at different stages of degeneration. For WT animals, purely pON responses accounted for 32% of the responsive neurons we recorded from. For p90-140 RCS animals (90-140 days post-natal, or after birth), this fraction went up to 68% and for p300-400 animals, 89% of the responses to electrical stimulation did not have any OFF component anymore (Table 3.1.1). In the WT retina, among OFF-center RGCs (identified from a binary white noise stimulus, Methods), 56% responded as purely pON, while 22% responded as pON-OFF and 22% as pOFF cells. OFF-center RGCs responded primarily (83%) as pON-OFF cells, with another 14% responding as pON cells and the other 3% responding as pOFF cells (Table 3.1.2).

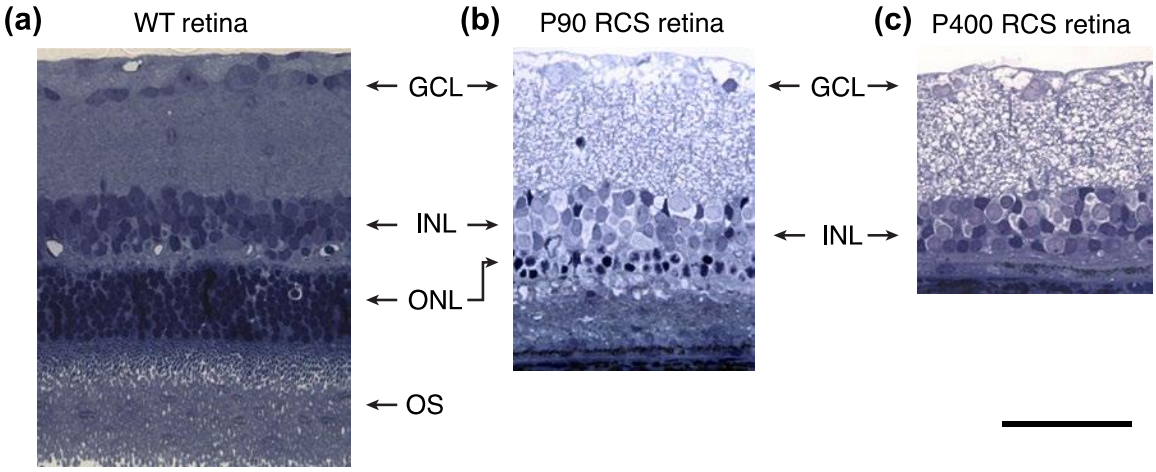

Figure 3.1.4 Histological analysis of the RCS rat retina. a) In the healthy WT retina, photoreceptor outer segments (OS) transduce light and modulate the membrane potential of photoreceptor somas located in the outer nuclear layer (ONL). Photoreceptors transmit neural information to cells in the inner nuclear layer (INL), which then relay it to the ganglion cells (GCL). b) In the P90 RCS retina, the outer segments have been replaced by debris, and only a fraction of the photoreceptors somas

remain in the INL. c) At P400, all the photoreceptor somas are gone from the RCS retina and only the INL and GCL remain. Scale bar: 50µm.

The reduction in the fraction of pOFF responses with time indicates photoreceptor involvement in their generation. Histological analysis of the WT and RCS retina (Figure 3.1.4) reveals that while the photoreceptor outer segments have degenerated by P90 in the RCS retina, a significant fraction of the photoreceptor somas remain, which could account for the remaining pOFF responses at P90. At P400, the photoreceptor somas are virtually all gone, as is the pOFF component of the response.

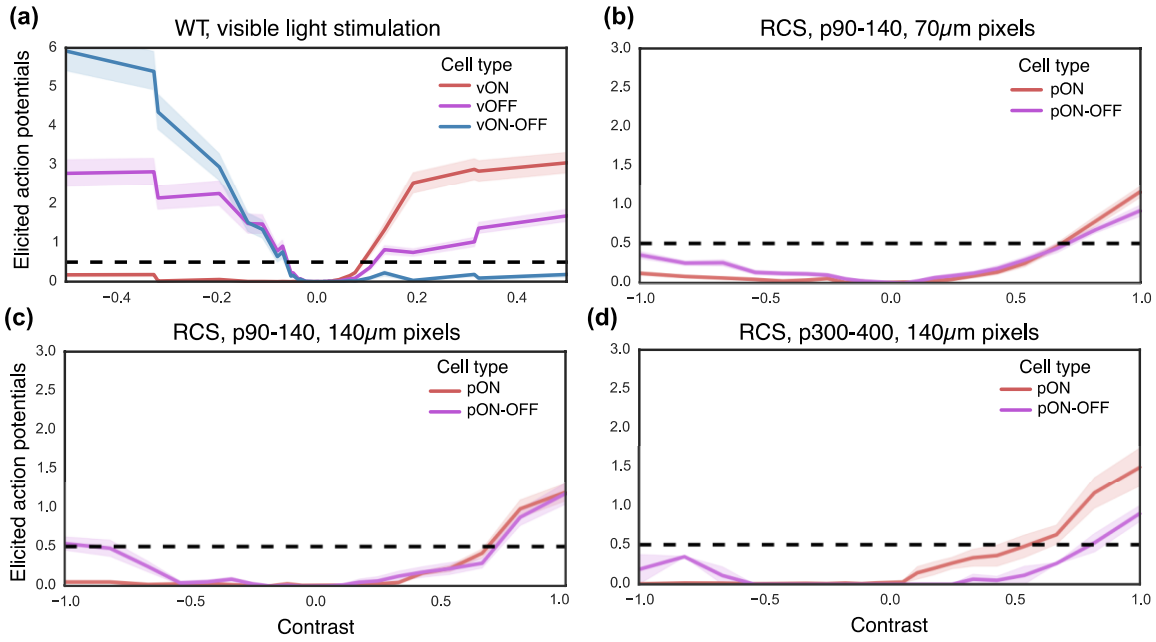

Figure 3.1.5 Mean population responses to contrast steps. a) WT responses to visible full field light steps could broadly be classified into vON (red), vOFF (blue) and vON-OFF (purple) responses. The black dashed line outlines the stimulation threshold, defined as a 50% probability of eliciting an action potential correlated with the contrast step. On average, ON cells responded to contrast increments greater than 7%, while OFF cells responded to contrast decrements as small as 3%. b) Photovoltaic

stimulation of p90-140 RCS retina with 70µm pixel implants requires 67% contrast steps to elicit responses in the RGCs. Maximum amplitude of the response is lower than with visible light in the WT retina. Contrast sensitivity curves are very similar with c) 140µm pixels used to stimulate p90-140 RCS retina and d) in advanced stages of retinal degeneration (p300-400 RCS rats). Confidence band represents the standard error of the mean.

Plotting the mean population response to contrast steps (Figure 3.1.5) reveals two striking features of prosthetic vision, compared to natural light responses: (1) dynamic range of the responses is considerably reduced, and (2) very large contrast steps are required to elicit reliable responses in the RGCs.

We defined stimulation thresholds as a 50% probability of eliciting an action potential (56; 30; 44; 37), as described in Methods. For visible light stimulation, the mean stimulation threshold was 7% positive contrast for vON cells, and 3% negative contrast for vOFF cells. When stimulating p90-140 and p300-400 RCS retina with either 70µm or 140µm pixels, stimulation threshold was reached between 56% (p300-400 RCS retina, 140µm pixels) and 70% (p90-140 RCS retina, 140µm pixels) contrast. The maximum amplitude of the response was on average 3.6 action potentials per contrast step for vON responses of the WT retina and 7.2 action potentials per contrast step for vOFF responses (Figure 3.1.5a). The amplitude of the response was significantly reduced in prosthetic stimulation of degenerate tissue, with only 1.2 action potentials per contrast step for stimulation of p90-140 RCS, in the pON response. Since pOFF and pON-OFF responses in degenerate tissue largely

disappear at the later phases of degeneration, we will ignore the few neurons that were detected as pOFF or pON-OFF in RCS tissue in further analysis.

	WT	RCS, p90-140	RCS, p300-400
pON	32%	68%	89%
pON-OFF	56%	30%	7%
pOFF	12%	2%	4%
Cell count	75	156	28

Table 3.1.1: **Prevalence of pON, pOFF and pON-OFF responses in different animal models.**

	OFF-center	ON-center
pON	56%	14%
pON-OFF	22%	83%
pOFF	22%	3%

Table 3.1.2: **Mapping visible light responses to prosthetic responses.**

While electrical stimulation of the healthy retina shows evidence of at least three types of responses to contrast steps (pON, pOFF and pON-OFF), the pOFF component of those responses can be explained by electrical stimulation of the photoreceptor layer. Electrical stimulation of the photoreceptors depolarizes them, thereby triggering action potentials at the onset of electrical stimulation in the OFF pathway, since photoreceptors naturally depolarize when struck with light (Figure 3.1.6, a).

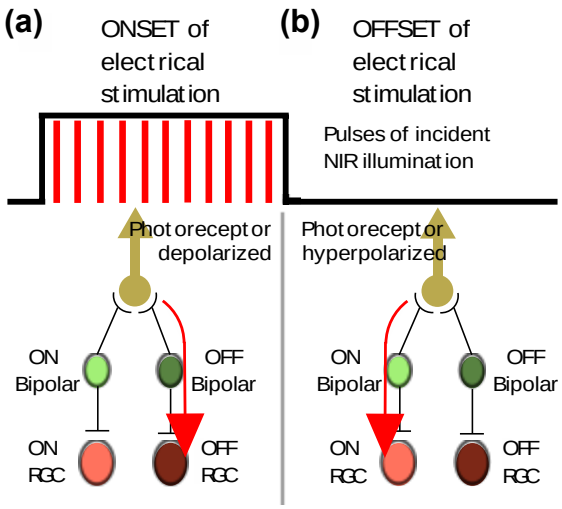

Figure 3.1.6 The pOFF responses can be explained by electrical stimulation of the photoreceptors. Electric fields should depolarize photoreceptors, thereby triggering response at the onset of electrical stimulation in the OFF pathway (a). When electrical stimulation stops, the photoreceptors should hyperpolarize again, causing an electrical OFF response in the ON pathway (b). Amacrine cell-mediated effects further complicate the OFF response. However, its progressive decrease with advancing degeneration correlates with disappearance of the photoreceptors (Figure 3.1.5), indicating that pOFF response is mediated by photoreceptors.

When electrical stimulation stops, the photoreceptors should hyperpolarize, causing an electrical OFF response in the ON pathway this time (Figure 3.1.6, b). With full-field stimulation of the rat retina, additional amacrine cell-mediated network effects further complicate the response. This makes it difficult to conclusively pharmacologically dissect the mechanisms behind the electrical OFF response. However, its progressive and almost complete disappearance as degeneration advances, correlated with disappearance of the photoreceptors in the RCS retina, strongly indicates that it is indeed mediated by photoreceptors.

We did not observe a difference in contrast sensitivity between implants with 70µm and 140µm pixels, indicative that while stimulation thresholds are affected by pixel size (36, 40), the contrast sensitivity function itself does not change once the retina adapts to above-threshold stimulation levels. The contrast sensitivity did not degrade with age of the degenerate retinas (p90-140 vs. p300-400) despite significant changes in the retinal network (41).

3.1.3 Implications for patients' experience

Bypassing the photoreceptors with subretinal electrical stimulation has strong implications on contrast sensitivity and dynamic range of prosthetic vision (23). Light stimulation of the photoreceptors leverages a finely tuned amplification cascade that can trigger responses to very dim illumination (a few photons only, (3; 53)), or to minute changes in contrast (62). Prosthetic subretinal stimulation of the inner nuclear layer in the degenerate retina elicits responses with, at best, twice smaller amplitude and ten times lower contrast sensitivity than normal. Contrast changes of at least 60% in Michelson units are required to elicit reliable responses, as compared to the 7% change required for vON responses and 3% for vOFF responses with natural vision.

We did not observe a difference in contrast sensitivity between implants with 70µm and 140µm pixels, indicative that while stimulation thresholds are affected by pixel

size (40; 36). The contrast sensitivity function itself does not change once the retina adapts to above-threshold stimulation levels at high frequency (>20Hz). The contrast sensitivity we measured matches values previously observed in-vivo (36), and, importantly, it did not decline with age of the degenerate retinas (p90-140 vs. p300-400) despite the expected changes in the retinal network (41).

Subretinal stimulation preserves a few important features of retinal signal processing, such as flicker fusion and transient responses to slower changes in luminance, as well as non-linear integration across subunits of RGCs with large receptive fields (37). However, disappearance of the electrical OFF responses means that both the ON and OFF pathways are activated simultaneously, a very unnatural stimulation paradigm. Indiscriminate activation of all the cells in the inner nuclear layer is likely to contribute to reduced contrast sensitivity since both excitatory bipolar and inhibitory amacrine cells could be driven by the prosthesis. It remains unclear how this phenomenon affects phosphene perception, since current clinical trials with subretinal prosthesis demonstrated that patients see phosphenes primarily as light rather than dark flashes, and can perceive patterns of stimulation (60).

The full-field measurements of contrast sensitivity we conducted do not take into account contrast improvements at higher spatial frequencies (images with finer details) due to center-surround effects in normal vision (17). It is reasonable to expect

this effect to be less pronounced with a subretinal prosthesis than with normal vision since horizontal cells responsible for part of the center-surround effects in the retina are thought to only synapse directly onto photoreceptors which disappear with degeneration, and not bipolar cells (32). Therefore, only lateral inhibition from the amacrine cells should be able to contribute to center-surround effects with subretinal prosthetic stimulation.

Making predictions about the human visual system based on measurements with a degenerate rat retina is difficult, given the major differences between the visual systems of the two species. The midget, parasol and small bistratified cells that dominate the human visual pathways (14) have no anatomical equivalence in rat. Differences in the rate and extent of retinal degeneration between humans and various animal models make it even more difficult to predict responses to electrical stimulation in human patients.

An important consequence of the reduced contrast sensitivity and lack of OFF responses with prosthetic vision is that efficiency of fixational eye movements (FEMs) for image refreshing and prevention of perceptual fading (45) is greatly diminished, compared to natural vision. While it is possible to deliver information with relatively high spatial content through the implant (37), most static visual scenes are not sparse enough to elicit responses in RGCs with FEMs alone. This

phenomenon could be responsible for the perceptual fading at high stimulation frequencies reported in patients with the subretinal implant Alpha-IMS, when FEMs which appear normal with the implant turned on (24) would be expected to trigger retinal responses. Patients prefer stimulation frequencies not exceeding 7Hz (59; 24) – well below the flicker fusion frequency, so the pulses introduce strong temporal contrast in the visual pattern. Lack of contrast sensitivity appears to be an important limitation of subretinal prosthetic devices that can strongly impede their ability to deliver visual information efficiently to the brain. This could be partially mitigated by pre-processing of the images between the camera and the implant, which by increasing local image sparsity could bring local contrast above stimulation thresholds.

3.2 Spatial resolution

3.2.1 Single-pixel stimulation distance thresholds

One way in which we characterized the spatial resolution of the prosthesis relied on *in-vitro* stimulation of individual pixels at low 2Hz frequency, while examining the spread of retinal stimulation around that pixel. We measured the spread of the retinal response as a function of the intensity and duration of the NIR pulses.

We found that the number of spikes elicited by a NIR pulse decreases for cells located further away from the illuminated pixel. A 1D gaussian function centered on the illuminated pixel and fitted to the number of spikes detected onto surrounding RGCs yields an approximation of the distance over which stimulation spreads (Figure 3.2.1).

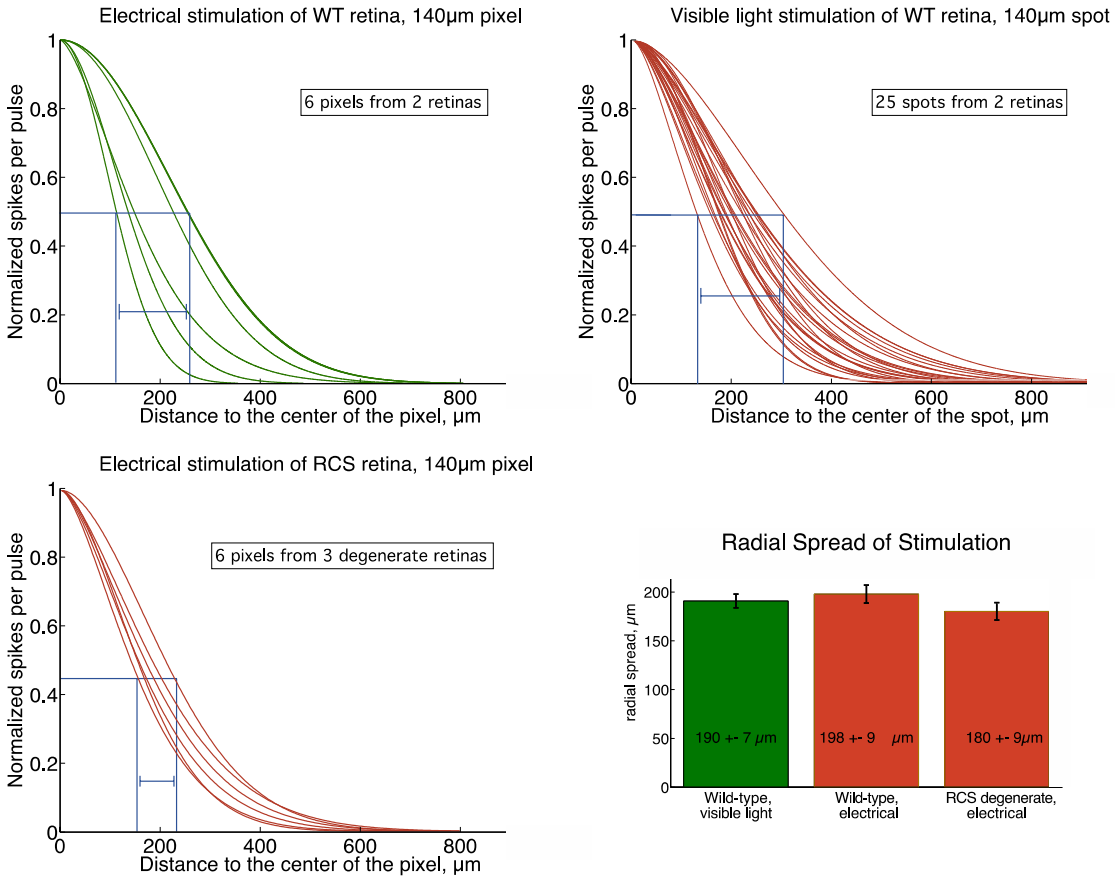

Figure 3.2.1 Radial spread of stimulation. The normalized spikes per pulse are plotted against the distance from the center of the stimulated region, depicted with a vertical shaded bar in each panel. There were similar spreads in stimulation d) between a) prosthetic stimulation in WT retina, b) prosthetic stimulation in RCS degenerate retina, and c) visible light stimulation in wild type retina. The error bars shown in (d) depict the standard error of the mean.

The results are compared with the response of a wild type (WT) rat retina to visible light stimulation with the spots of the same size (Figure 3.2.1c) On average, the number of elicited spikes decreased by 50% around a distance of 200 microns from the center of the stimulated region. This range is comparable with that of visible light stimulation in the WT retina, although this distance is not an accurate reflection of the maximum spatial resolution achievable by the implant. The low frequency of

stimulation and the localized illumination means that faint signals are more easily detected by distant RGCs, in the absence of the lateral inhibitory effects present in a more dynamic, noisy stimulus (See Chapter 3.3).

3.2.2 Electrical receptive fields, as measured with sparse white noise

Another way to measure the lateral spread of electrical stimulation is by observing the size and shape of the electrical receptive fields (eRF) of individual RGCs. By projecting a pseudo-random stimulus of black and white pixels, it is possible to ask of the neuron: "On average, what do you see right before you are provoked to fire an action potential?" In this way, the STA can be constructed by averaging the last few frames before each action potential, to give an idea of that cell's preferred stimulus (Methods, (10)). When the following analysis was conducted, we were constrained to using stimuli that were predictable and repeatable, in order that the electrical artifact could be removed. Therefore we were unable to show a high-frequency dynamic white noise stimulus, so we instead projected small NIR spots onto each pixel on the implant, one at a time, to determine which pixels were able to elicit responses from each detected RGC. We compared the results to the visual receptive fields (vRF) obtained from visible light white noise stimulation of WT retina. When we later improved the artifact removal process it allowed for us to project more complex stimuli (Methods). A high-frequency version of this stimulus with multiple pixels stimulated simultaneously is discussed in Chapter 3.3.

The rest of this chapter 3.2 contains modified versions of our previously published work (23):

For each neuron, we constructed a STA showing the pixels which were able to elicit responses from that neuron reliably (>.5 spikes per pulse) in white, and the others in gray or black (Figure 3.2.2b).

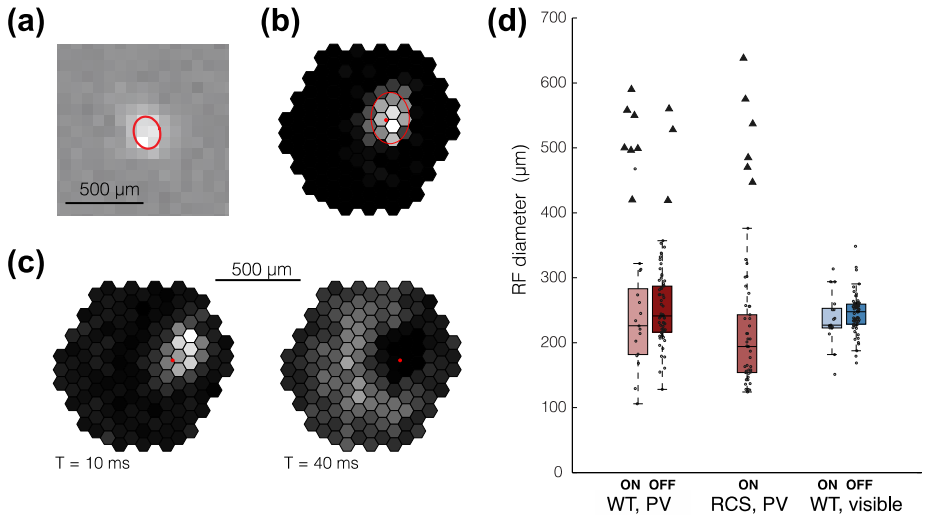

Figure 3.2.2 (a) A typical visual receptive field (vRF) for RGC in a WT rat retina obtained from analysis of a white noise stimulus is comparable in size to an electric receptive field (eRF) (b). The strength of the cell's response to each pixel, measured in the number of spikes elicited per light pulse at 2Hz, is encoded in gray levels. (c) Example of small subset (16/140) of abnormal RFs with diffuse components, plotted as triangles and discarded from the average RF sizes shown in d), where no significant difference in RF sizes was observed between photovoltaic and visible responses.

The average eRF diameter was 248±59µm in WT and 203±63µm in degenerate RCS retinas (Figure 3.2.2d). With visible light, the average diameter of the WT vRFs was 244±32µm (Figure 3.2.2d), not significantly different from the measured eRF sizes. Despite recording from a wide variety of RGCs in WT retina (ON and OFF, transient

and sustained, brisk and sluggish cells (9)) with a variety of RF diameters, we did not observe any significant correlation between eRF and vRF sizes.

Some eRFs in both the WT and RCS retinas (16 out of 140 neurons) had a more complex structure, displaying a localized and a diffuse, donut-shaped component. Both of them exhibited excitatory response, but with different latencies (Figure 3.2.2c). These eRFs with a diffuse component were not included in the eRF average size (Figure 3.2.2d, triangles).

3.2.3 In-vitro and in-vivo alternating gratings

While measuring the spatial extent of electrical receptive fields obtained with a sparse white noise provides an indication of achievable spatial resolution, it does not take into account possible non-linear effects of presenting more complex stimuli. In order to account for this, we characterized retinal responses to alternating square gratings of various spatial frequencies using visible light and photovoltaic stimulation (see Methods). This type of stimulus is routinely used for measuring visual acuity in-vivo (50; 19; 15). Experiments were conducted with RCS retinas for photovoltaic stimulation (4 ms, 5 mW/mm^2 NIR pulses) and with WT retinas for visible light stimulation (10 ms, 591 nm pulses, low photopic regime), and the width of the square-wave grating stripes varied from 7 to 300µm. Visible and NIR images were projected with 20Hz flicker frequency and 1Hz grating alternation.

Electrical stimulation of the RCS retina resulted in a continuum of responses, ranging from a combination of strong transient (flicker-fused) response to the alternating grating with very weak response to individual pulses at 20Hz, to more robust responses to every stimulation pulse.

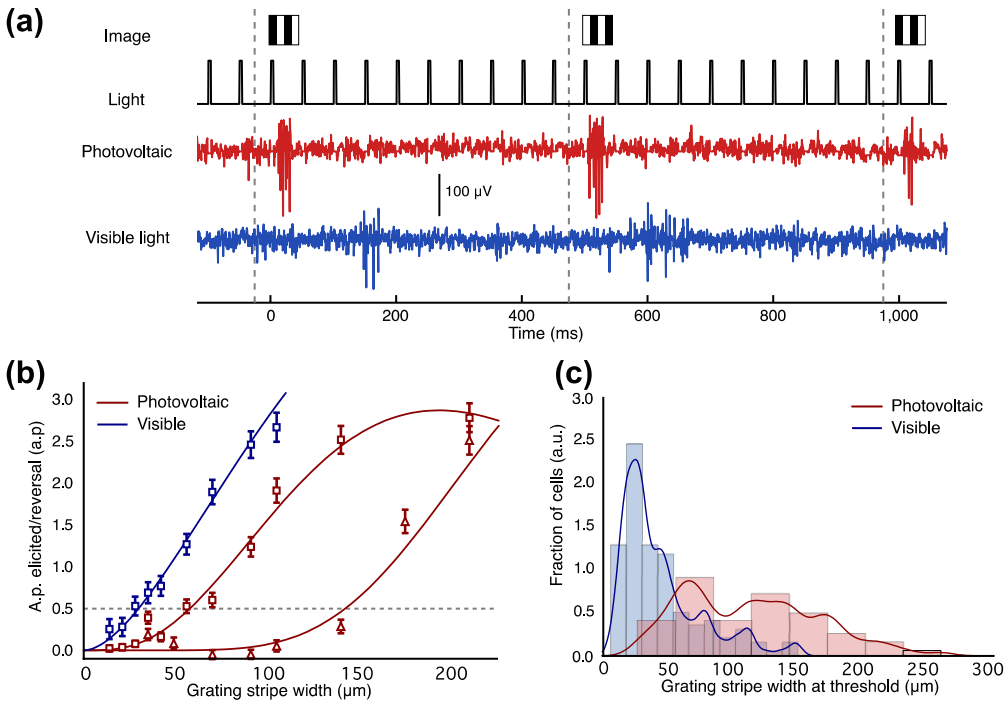

Figure 3.2.3: Response of RGCs to alternating gratings. a) Light is pulsed at 20Hz, while grating contrast is reversed at 2Hz, triggering ganglion cell responses to photovoltaic (red) and visible light (blue) stimulation. These RGCs do not response to individual light pulses but only to the 2Hz image alternation. The photovoltaic response was recorded from a RCS retina and the visible response was recorded from a WT retina. b) Amplitude of the response to grating contrast reversal as a function of the grating stripe width, illustrated for a neuron activated by visible light (blue) and 2 neurons responding to photovoltaic stimulation (red). Stimulation threshold was defined as 50% probability of eliciting an action potential per grating alternation. Error bars show standard error of the mean. c) Histograms and kernel density estimates (solid fit lines) of the stimulation thresholds distributions for visible-light and photovoltaic stimulation. The peak in the visible-light threshold distribution occurs at

28μm. With photovoltaic stimulation, one peak occurs at 67μm, followed by a second peak beyond 100μm.

In the WT retina we observed very little, if any response to individual pulses of visible light at 20Hz, and strong response to the grating reversal. Thus a significant fraction (about half) of the RCS rat RGCs under electrical stimulation and virtually all WT rat RGCs under the visual stimulation responded to the contrast reversal of the gratings and not to every pulse of light (Figure 3.2.3a), illustrating the flicker fusion and adaptation to static images.

To assess the spatial resolution of the retinal response to photovoltaic and visible light stimulation, we quantified the strength of the RGC response to grating contrast reversal as a function of the spatial frequency (stripe width). This response, measured in spikes elicited per grating reversal, decreased with increasing spatial frequency of the gratings, both for visible light and electrical stimulation (Figure 3.2.3b).

Stimulation threshold was defined as the grating stripe size that resulted in a 50% probability of eliciting an action potential correlated with the grating contrast reversal (see Methods). The distribution of thresholds measured with visible light stimulation peaked at a stripe width of 28μm in one of the preparations and at a stripe width of 48μm in the other. The difference is most likely due to differences in eccentricity of the retinal sections we recorded from. With photovoltaic stimulation, the threshold

distribution exhibited a peak at 67μm per stripe, with a large tail extending to widths greater than 100μm (Figure 3.2.3c, 109 RGCs, 4 preparations).

Responses of the neurons to gratings smaller than their receptive field diameter, whether electrical or visible, can be explained by non-linear interactions in receptive field subunits (52; 39). For visible light, the peak corresponds to neurons responding to each phase of the grating alternation (Figure 3.2.3a). This classical doubling of the response is indicative of nonlinear spatial summation (52, 39), a crucial feature of natural vision that allows for ON and OFF responses within a receptive field subunit even if the total amount of illumination is maintained, but the orientation of illumination shifts from one side of the receptive field to the other. Similarly, neurons responded to gratings with 67μm stripe width in NIR with frequency doubling (Figure 3.2.3a). This demonstrates non-linear summation inside the RGC electrical receptive fields, with the size of the effective non-linear subunits comparable to our pixel width. 71% of RCS neurons that responded to grating stipe widths smaller than 75μm exhibited frequency doubling in their responses (min/max ratio of the peak of the response to each phase of the grating exceeding 0.75), consistent with non-linear summation in receptive field subunits.

Importantly, all neurons that exhibited complete flicker fusion with photovoltaic stimulation (i.e., no response to 20Hz pulses without the change of the projected

image) responded to gratings stripe widths smaller than 100µm, suggesting that flicker fusion might be a crucial mechanism for restoring high visual acuity.

In-vivo Measurements

In-vivo experiments performed by our collaborators at Stanford University confirmed this result with cortical recordings of wild-type rats who were previously implanted with the 70um, 2 diode prosthetic devices (37). Visually-evoked potentials (VEP) were recorded at the cortex of the sedated RCS rats, while the contrast-reversing gratings stimulus was delivered to the implanted prosthesis. The VEPs decreased in amplitude with decreasing spatial period of the stimulus, until the signal was no longer discernible in the cortex (Figure 3.2.4a). They recorded the cortical responses to such alternating NIR patterns in implanted RCS rats and to the same patterns presented with visible light in WT animals outside the implanted area. The square-wave grating patterns were projected using 4 ms pulses at 40Hz repetition rate, reversing the contrast at 1Hz. Grating stripe width varied from 6µm to 200µm.

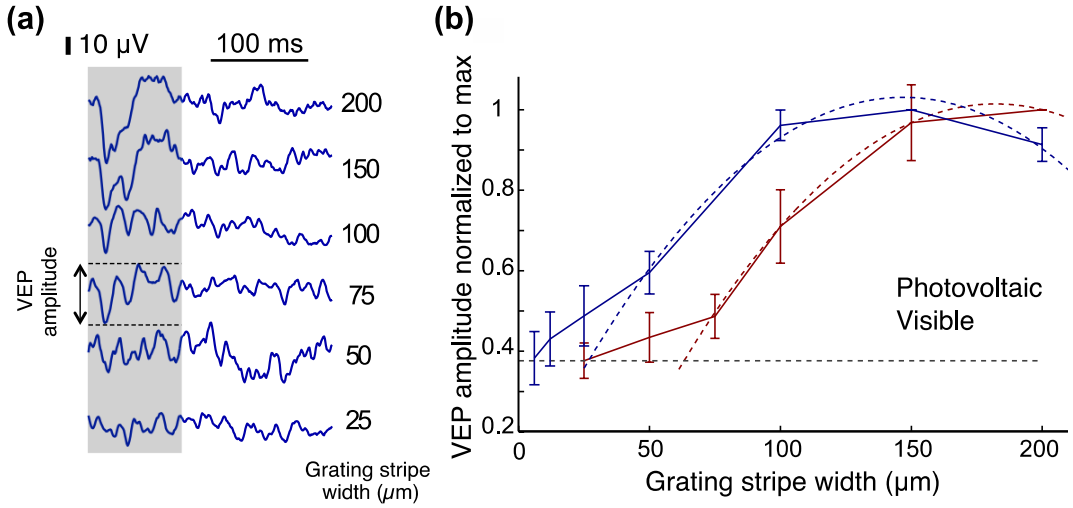

Figure 3.2.4: In vivo prosthetic stimulation and visual acuity. a) Sample VEP traces corresponding to different grating stripe widths. Responses decrease to the noise level with 50µm stripes. b) Amplitude of the cortical response to visible gratings (blue) exhibits maximum at 150µm per stripe, and decreases to the noise level with stripes narrower than 25µm. With prosthetic stimulation (red), the VEP amplitude follows a similar curve, with a signal for 50µm/stripe becoming not significantly different from the noise. Acuity limit, estimated as a crossing point of the parabolic fits to the VEP data with the noise level (dashed lines), corresponds to 29µm/stripe for visible gratings and 63µm/stripe for prosthetic stimulation. Error bars show standard error of the mean.

The VEP amplitude decreased with increasing spatial frequency for both visible and electrical stimulation (Figure 3.2.4b). Extrapolation of the measured data down to the noise level yielded an estimate of the acuity limit of 63µm/stripe or 0.48 cycles per degree (cpd) for prosthetic stimulation, compared to 29µm or 1cpd for normal vision in rats, and compared to our in-vitro result of 67µm/stripe. If the spatial localization from our measurements will translate to the human retina, such prosthetic performance would correspond to visual acuity of 20/250, which is well below the legal blindness limit of 20/400, as defined by the World Health Organization (68). With the enhanced acuity provided by eye movements (31) and perceptual learning in human patients, visual acuity could perhaps cross the 20/200 threshold of legal

blindness in the US.

3.3 Spatio-temporal responses to high-frequency electrical white noise

In order to examine the spatio-temporal response properties of retinal tissue subjected to photovoltaic subretinal stimulation at naturalistic frequencies, we used hexagonal white noise electrical stimulation as described in Methods. For each piece of degenerate retina (3 preparations), we recorded 4000 seconds of hexagonal white noise electrical stimulation, and for each piece of WT retina (4 preparations), we collected visible light white noise for classification of cell types, in addition to the same electrical stimulation. We obtained the spike-triggered averages, receptive fields, and time courses for both types of stimulus, and determined that there are distinct cell classes for electrical responses, analogous to the visible light responses. Some cells responded only to the onset of electrical stimulation (pON), and some responded only to the offset (pOFF). In WT retina, the majority of pON responses came from OFF-center cells, and vice-versa. It is significant and promising for future patients that the prosthesis is able to resolve high-frequency stimulus, and suggests that the amount of temporal pre-processing of the images delivered through the goggles may be minimal, though as evidenced in the section on contrast sensitivity, it is likely that the contrast will need to be enhanced. A more in-depth analysis of the

results of this stimulus is discussed in the following sections.

3.3.1 RGCs can respond to complex spatio-temporal patterns at high stimulation frequencies.

The rest of this chapter 3.3 is a modified version of our previous work (58):

We characterized the responses of RGCs to complex visual stimuli in three degenerate (RCS) retinas by activating the photovoltaic implant placed subretinally with a 20Hz frame rate binary white noise movie. The movie had 70μm hexagonal pixels, which were aligned with the hexagonal photodiode pixels of the implant (see Methods).

For 32 RGCs, spike-triggered analysis of the white noise stimulus yielded statistically significant responses with a signal to noise ratio of at least 3 (see Methods), indicating that the implant successfully elicited responses in the RGCs despite the rapidly varying spatio-temporal structure of the stimulus (Figure 3.3.1). The photovoltaic spike-triggered averages (pSTAs) are the prosthetic equivalent of the classical visual spike triggered averages, which approximate the temporal characteristics and spatial localization of the RGC receptive fields. pSTAs were spatially localized and had photovoltaic ON (pON) responses, evidenced by the positive pSTA value of the first time course peak preceding the spike (see Methods). This result is consistent with direct depolarization of the bipolar cells by the electrical

stimulus. An example pSTA receptive field and its time course are shown in Figure 3.3.1a. pSTAs were similar between the three retinas (Figure 3.3.1b).

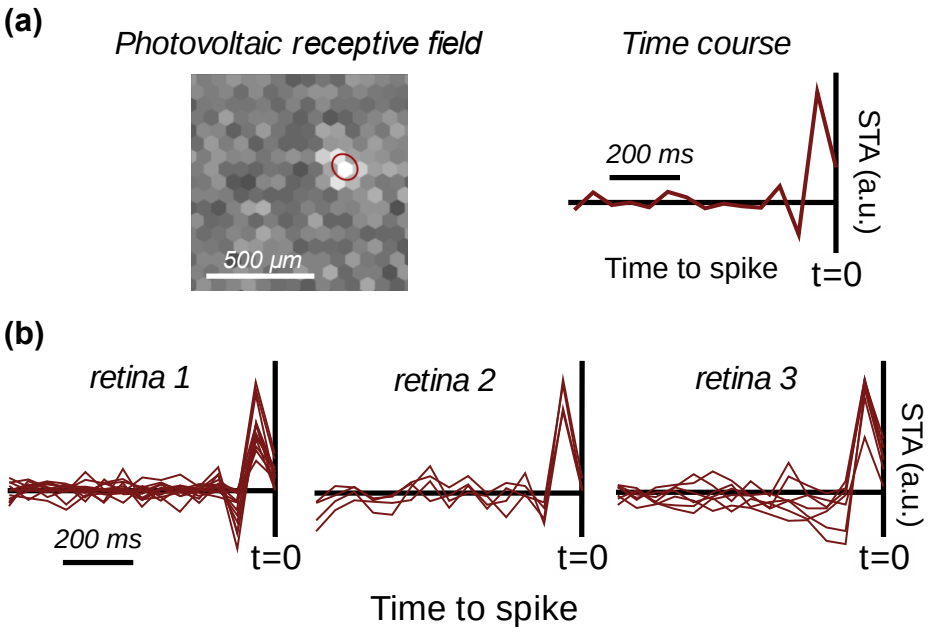

Figure 3.3.1 Photovoltaic spatio-temporal response properties of the RGCs in RCS retinas.
a) Photovoltaic responses of an example pON RGC in RCS retina. Top panel shows the receptive field and the adjacent panel the corresponding STA time course. b) Overlaid time courses of all of the RGCs detected in three separate retinal preparations. All of the RGCs have typical pON responses.

The average receptive field diameter was 205±14µm, in line with the values previously reported in the literature for low-frequency sparse binary white noise stimulation of the rat retina (6). We estimated the average response latency as the time between the spike and the first zero crossing of the pSTA time course that preceded it (see Methods). In the linear nonlinear model of RGCs, this duration corresponds to the delay of the cell's maximum response to the light step of preferred

polarity (increase in light level for an ON and decrease for an OFF RGC) (10). On average, across three RCS retinas, response latency was 88±5ms.

3.3.2 Comparison of photovoltaic and visual responses

In order to compare RGC responses to photovoltaic and to visual stimulation in healthy retina we applied both the visual and photovoltaic white noise stimuli to each retinal preparation. The photovoltaic stimulus was identical to the one used in RCS rats. The visual white noise had 60μm size square pixels and was refreshed at 30Hz frame rate (see Methods). Visual STAs (vSTAs) and photovoltaic STAs (pSTAs) were again obtained by reverse correlation analysis between the RGC spike trains we recorded and the stimuli delivered to the retina (Figure 3.3.2). Response latency estimated from the STA time courses was shorter for photovoltaic than for visual stimulation (68±5ms vs. 179±45ms, respectively). The faster response to photovoltaic stimulation is likely due to bypassing the phototransduction cascade present in normal vision, and is consistent with observations previously reported in the literature (44; 40).

We classified RGCs based on their vSTAs into ON- and OFF-center types (Figure 3.3.2a,b). We used the unique electrical images (EIs) of the RGCs (50; 34) to match cells between the visual and prosthetic stimuli (see Methods). The average receptive

field diameter of the photovoltaic responses was 191±9μm, compared to 228±10μm for the visual receptive fields of the same RGCs. Unlike the RCS retina, here we observed RGCs with both pON and pOFF pSTAs (Figure 3.3.2). While some of the RCS time courses had triphasic shape with three peaks (Figure 3.3.1b), this feature was more pronounced in WT photovoltaic time courses. Polarity of the photovoltaic RGC responses was reversed relative to the visual ones, i.e. visual ON (vON) RGCs behaved as photovoltaic OFF (pOFF), and vOFF RGCs behaved as pON cells (Figure 3.3.2a,b). Virtually all recorded RGCs exhibited this reversal across the 4 retinas we characterized. Time courses from the two typical recordings are shown in Figure 3.3.2c.

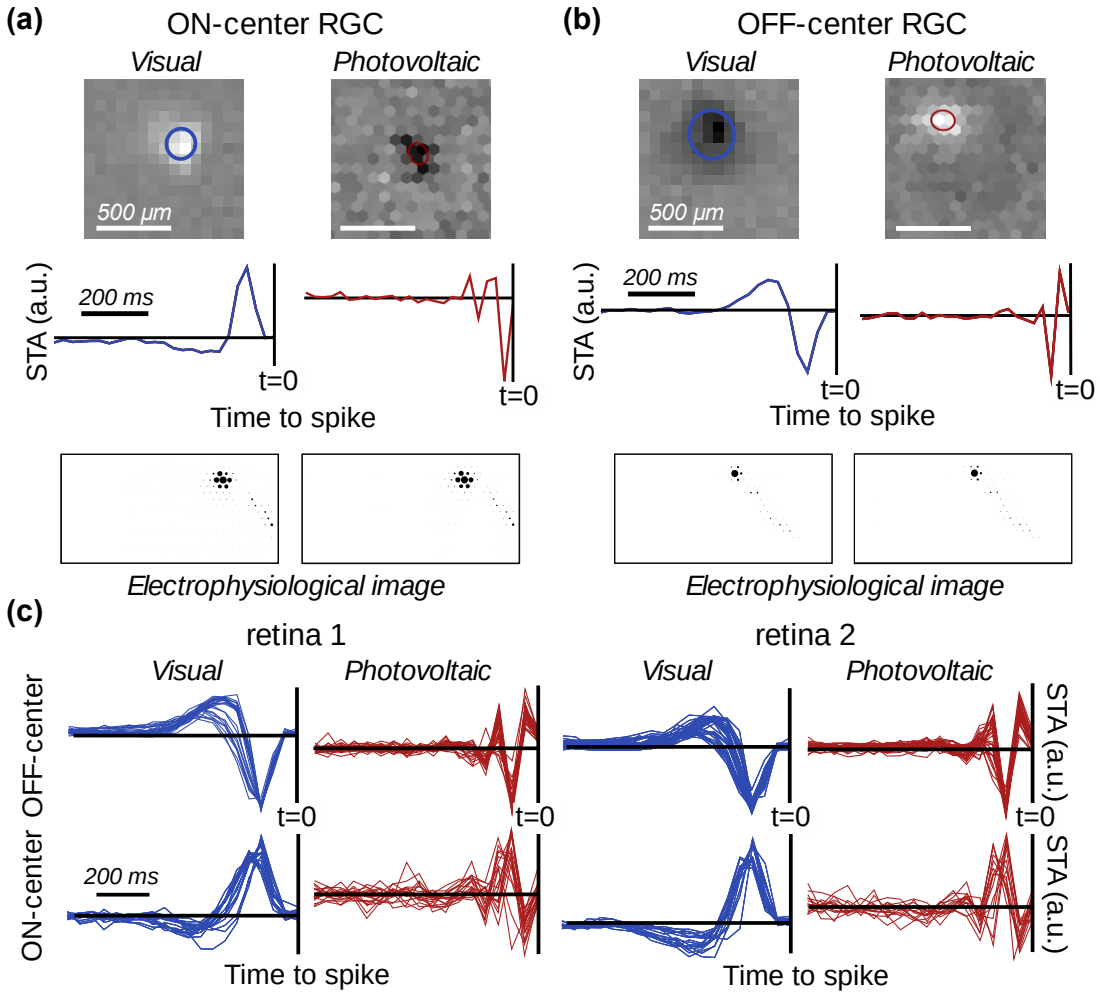

Figure 3.3.2 Visual and photovoltaic spatio-temporal response properties of RGCs in the healthy retina. a) Responses of an example ON-center RGC. Top panels show receptive fields elicited by the visual and photovoltaic stimulation and the middle panels the corresponding STA time courses. Polarity of the photovoltaic response is opposite to that of the visual response: the visual ON cell (vON) becomes photovoltaic OFF cell (pOFF). The lower panels show the identical electrophysiological images of RGCs responding to visual and electrical activation (see Methods) confirming that the responses of the same RGC were measured. Ellipses overlaid on the receptive field panels correspond to the 1-sigma contours of the 2-d Gaussians fitted to the receptive fields. b) Responses of an example OFF-center RGC. The response polarity is again reversed with the vOFF becoming the pON RGC. c) Overlaid time courses of all of the RGCs detected in two separate retinal preparations. In each preparation the RGCs were divided into vON and vOFF types according to their visual responses. The response polarity was reversed for all of the cells when switching from visual to photovoltaic stimulation.

A possible source of this reversal is the opposite response of photoreceptors to electrical and light stimuli, as shown in Figure 3.1.6. Cells are depolarized by electrical stimulation, but photoreceptors hyperpolarize when illuminated by light. Depolarization of photoreceptors normally corresponds to a decrease in illumination, and hence the retina interprets electrical activation of the photoreceptors as a decrease in light intensity. Thus, an increase in the electrical stimuli mimics a decreasing light level, while a decrease in electrical stimulation has the same effect as an increase in the light intensity. Consequently, normal signaling from photoreceptors to the ON and OFF-bipolar cells should lead to reversed responses with photovoltaic stimulation: pOFF responses of the vON ganglion cells and pON responses of the vOFF ganglion cells. In the RCS retina, this stimulation mechanism is absent due to the loss of photoreceptors and their sign-preserving or sign-inverting synapses to bipolar cells.

To test this hypothesis, we used a mixture of 100μM concentration of mGluR6 receptor antagonist LY 341495 and 150μM l-AP4 mGluR6 agonist (l-2-amino- 4-phosphonobutyric acid) to selectively block synaptic transmission from photoreceptors to ON-bipolar cells (14). We then measured the photovoltaic response properties of the RGCs using full-field steps of +100% or -100% contrast (see Methods). Before application of the blockers, vON cells responded to positive contrast steps with 0.70 +/- 0.57 spikes elicited per step (+/- standard deviation, pON response), and to negative contrast steps with 1.26 +/- 0.45 spikes per step (pOFF

response). vOFF cells responded to positive contrast steps with 1.73 +/- 1.05 spikes per step, and did not respond to negative contrast steps (0.01 +/- 0.05 spikes per step). After application of the blockers, visual responses of the vON RGCs to the visual white noise disappeared, while the responses of the vOFF cells remained largely unchanged. Blocking the signal transmission from photoreceptors to the ON-bipolar cells led to the complete disappearance of the pOFF photovoltaic responses initially observed in vON RGCs, consistent with pOFF responses being caused by electrical polarization of photoreceptors. At the same time, pON responses of the vOFF RGCs remained, with 2.55 +/- 1.21 spikes elicited per positive contrast step.

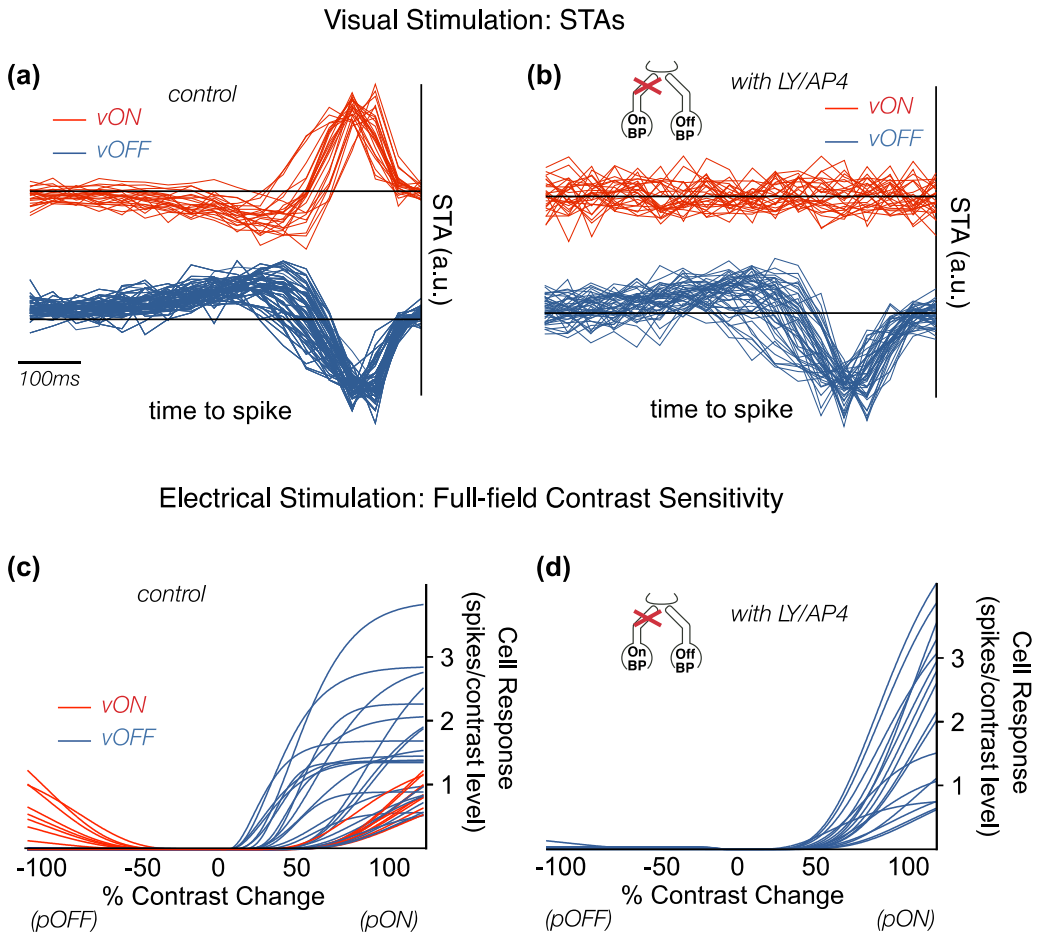

Figure 3.3.3 Application of pharmacological blockers. a) Normal vON and vOFF time courses. b) Application of mGluR6 receptor antagonist LY 341495 in conjunction with l-AP4 mGluR6 agonist selectively block the photoreceptor-to-ON bipolar synapses, eliminating the vON response to visible light. c) Contrast sensitivity profiles of individual vON cells (red) and vOFF cells (blue) in response to electrical stimulation, before the application of blockers. The y-axis shows the number of spikes per contrast level, each of which consisted of 10 NIR pulses over the period of .5 second. All of the pOFF responses are originating from vON cells. d) The same contrast sensitivity profiles after application of blockers, showing a disappearance of both vON cells responses and, correspondingly, their pOFF responses.

3.3.3 Opposing surround in photovoltaic responses.

The center-surround organization of the RGC receptive fields is one of the fundamental properties of vision (33). The classical surround mechanism is associated with negative feedback by the horizontal cells on the photoreceptor terminals (66; 47). Such feedback might result in the surround being present in the photovoltaic receptive fields of WT RGCs, but is expected to disappear after photoreceptor degeneration. However, amacrine cells also can mediate an opposing surround (66; 47) and if the retinal circuitry were to be preserved in the degenerated retina, this mechanism of the opposing surround could be preserved as well.

In order to test if an opposing surround is present in photovoltaic responses, we measured the surround and central signals in the following way: The center signal was estimated as the average (per pixel) STA time course for the pixels located within the 2-σ ellipse of the 2-d Gaussian fit to the receptive field. The surround signal was calculated as the average STA time course for the pixels located outside the central zone, in the (4-8)σ band for visual and (3-6)σ band for the photovoltaic STAs. The cutoff values were selected so as to avoid the region where the center signal switches to the surround while maximizing both center and surround signals. As expected, we observed opposing surround signals in both vON and vOFF vSTAs.

Figure 3.3.4a,b shows two example RGCs with visual surrounds having opposite stimulus preference (sign of the time course deflection preceding a spike) compared to their centers. We also measured opposing surround signals in the WT pSTAs (Figure 3.3.4c,d).

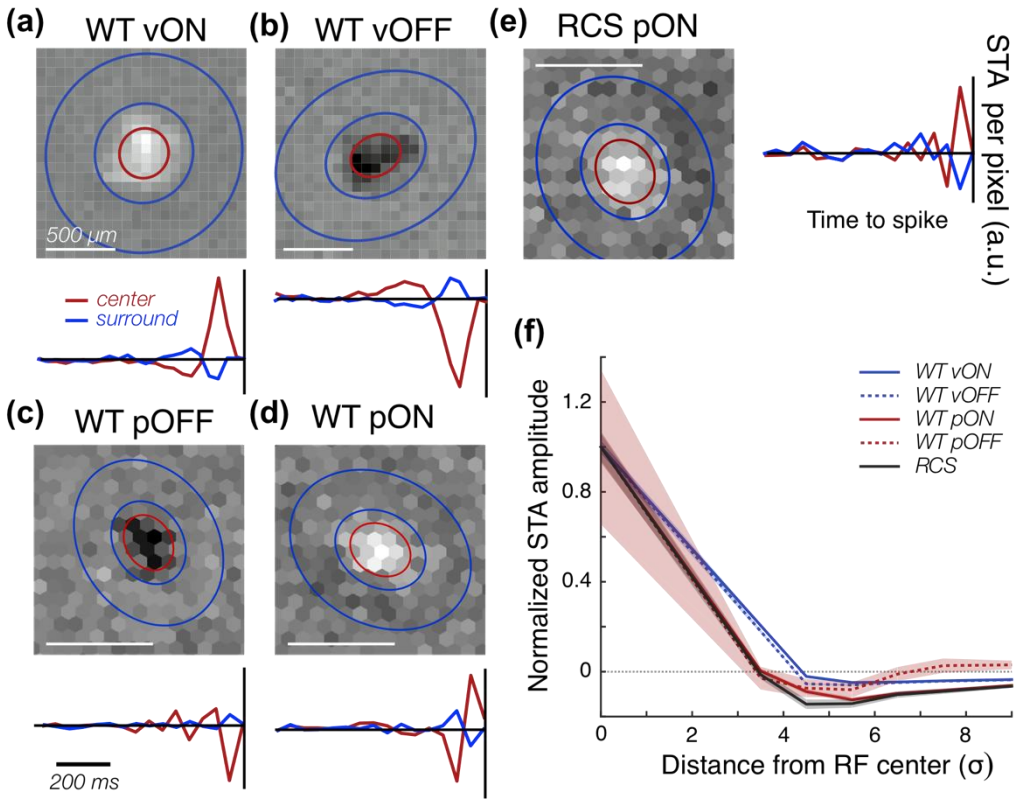

Figure 3.3.4 Center-surround organization of the receptive fields. a) The visual STA receptive field of an ON RGC in the healthy WT retina. The center and surround time courses are shown at the bottom of the panel. The center (surround) time course is calculated as the average time course of the pixels marked with red (blue) dots. Panels b), c), d) and e) show receptive fields as well as the center and the surround time courses calculated in the same way for visual response of the vOFF WT RGC, photovoltaic responses of the WT pOFF, pON, and RCS pON RGCs, respectively. f) STA response (peak time course deflection preceding the spike) vs. distance from the center of the receptive field. The curves represent the average responses of all the identified RGCs. The bands correspond to the standard error of the mean. The mean of each class of responses was normalized to the value in the center of the receptive field. Visual and photovoltaic OFF responses were inverted for the ease of comparison.

Surprisingly, the photovoltaic responses of the RGCs in RCS retina also had broader opposing response (Figure 3.3.4e). We quantified the strength and sign of the center and the surround by measuring the maximum time course deflection preceding the spike. We measured the spatial properties of the center and surround signals by calculating the STA response as a function of the distance from the center of the receptive field. Figure 3.3.4f shows that both visual and photovoltaic STAs have opposing surrounds that are wider than the center and become weaker as the distance from the center increases. Photovoltaic surrounds were stronger than visual ones, as measured by the ratio of the maximum surround amplitude to the center (Figure 3.3.4a, Table 3.3.1). The opposing surrounds of the RGCs in degenerate RCS retina were similar to those of the pON RGCs in the healthy retina. We noticed that cell-to-cell variability for both center and surround signals was larger for the WT pOFF RGCs than for pON RGCs in WT and RCS retinas. A possible explanation is that direct stimulation of the bipolar cells and photoreceptors has opposing effects on the pOFF RGCs. The balance between these two mechanisms determines the strength of the response leading to larger cell-to-cell variability than in the pON RGCs in WT and RCS retinas, for which both photoreceptor-mediated and bipolar cell-mediated stimulation mechanisms affect the cell in the same way. In summary, our measurements suggest that the center-surround organization of the receptive field is preserved with subretinal stimulation even in a degenerate retina that lacks photoreceptors.

	RCS pON	WT pON	WT pOFF	WT vON	WT vOFF
Receptive Field Diameter (μm)	205±14	208 +-9	176 +-6	227 +-7	235 +-7
Response Latency (ms)	88±5	60+-5	73 +-7	175+-10	157+-9
Surround/Center Response Ratio	-.15 ± .02	-.13 ± .01	-.08 ± .03	-.048 ± .003	-.060 ± .004
Distance between EI and RF centers (μm)	34±4	74±5		59±5	

Table 3.3.1 Comparison of visual and photovoltaic responses. Row 1: Average STA receptive field sizes for visual and photovoltaic responses. Row 2: Average response latency estimated from the photovoltaic and visual STA time courses. Row 3: Ratio of the strength of the surround response to the strength of the center response. Row 4: Offsets between receptive field center location and cell soma. See Methods section for the description of how the quantities in the table were calculated. All errors correspond to the standard error of the mean. Responses of 148 RGCs in the healthy retinas and 32 RGCs in the RCS retinas were used to calculate the averages.

3.3.4 Subretinal electrical stimulation preserves the retinotopic mapping.

Retinotopic mapping between RGC somatas and their afferents in the visual cortex is essential for proper image formation in the brain. If retinotopic mapping is not preserved in prosthetic vision, stimulation patterns can appear distorted to a patient, as in the case of axonal activation by epiretinal prostheses (49; 65). As shown above, the photovoltaic responses of the ganglion cells to high frequency binary white noise were spatially localized, with receptive field sizes similar to those obtained with visible light stimulation (Table 3.3.1). These results also matched receptive field sizes previously reported using low frequency sparse white noise stimuli (37).

We verified proximity between the receptive field center and the RGC soma by measuring the distance between the center of the functional receptive field and the RGC cell body location estimated from its electrical image (see Methods). The average displacement between the center of the receptive field and cell soma in photovoltaic stimulation of the RCS retina was 34±4μm, while it was about twice larger in the healthy retina (Table 3.3.1). Together with spatially localized STAs, these results suggest that retinotopic mapping is preserved with subretinal stimulation of both the healthy and the degenerate retina.

3.3.5 Significance of photovoltaic stimulus at high frequencies.

Preservation of the spatio-temporal response properties of individual RGCs in prosthetic vision is important in order to successfully restore vision to patients blinded by retinal degeneration. Natural vision relies on multiple parallel pathways in the retina, each corresponding to its own RGC type. While each of these pathways has its own spatio-temporal, and sometimes chromatic response properties, the following three features have been found to be almost universal among different types of the RGCs: (1) spatially localized receptive fields; (2) fast, ~100ms, response; (3) antagonistic center-surround organization of the receptive fields.

We find that RGCs in both healthy and degenerate retinas respond to photovoltaic spatio-temporal binary white noise at 20Hz frame rate. The spatial extent and temporal dynamics of the receptive fields are similar between the visual and photovoltaic responses. Antagonistic center-surround organization of the photovoltaic receptive fields is present in both healthy and degenerated retinas. Stimulation of the photoreceptors in healthy retina leads to distinct photovoltaic responses of the ON- and OFF-center RGCs, opposite to their responses to visual stimulation. However, this selectivity disappears with photoreceptor degeneration, leaving only ON responses to photovoltaic stimulation in degenerate retina, limiting the utility of such a selective activation. These findings and their implications are discussed below.

It has been shown previously that spatially simple (full-field or 1-dimensional reversing gratings) and temporally slow (2Hz) amplitude modulation of high frequency (20 to 40Hz) trains of photovoltaic pulses resulted in transient responses of the retinal ganglion cells to slow changes in light intensity (37; 23). These results indicate that subretinal photovoltaic stimulation preserves flicker fusion and adaptation to static images. It was also reported that retinal network-mediated responses can be elicited by 25Hz electric epiretinal stimulation with static spatial distribution, but stochastic temporal changes in amplitude, indicating that fast changes in the full field stimulation can elicit responses in the presence of flicker fusion (53).

We demonstrate for the first time that the retina responds to spatio-temporal white noise stimulation delivered through a photovoltaic subretinal prosthesis at 20Hz frame rate. Retinal response to complex spatial and fast temporal patterns exhibited many similarities to natural visual response.

3.3.6 Implications of spatio-temporal properties of photovoltaic response

Localized RGC receptive fields are essential for the transmission of spatial information to the brain. We observed that the size of the receptive fields was similar between photovoltaic and visual responses in the healthy retina. This size did not increase in the degenerate retina, which is consistent with our previous results obtained with a slow sparse white noise stimulus, where a single random pixel was illuminated in each frame of the 2Hz frame rate (37). Our current measurements demonstrate that spatial localization is preserved in response to a more dynamic and complex stimulus. Furthermore, we show that the photovoltaic receptive fields of individual RGCs co-localize with their cell bodies, thereby preserving the topological mapping between the inputs into the retina and their representation in the brain. This is an important feature of the network-mediated retinal responses. Direct activation of RGCs by epiretinal implants was shown to disturb this mapping through direct activation of axons resulting in distorted visual percepts (49; 65).

Temporal response properties of the RGCs as measured through the STA time course confirm that the photovoltaic response has shorter latency than the visual one (44; 40), most likely because it bypasses the phototransduction cascade in the photoreceptors. The latency of the photovoltaic responses in the healthy retina was somewhat shorter than in the degenerated retina (Table 3.1). The difference might be caused by the different mechanisms of the stimulation that involve both photoreceptors and bipolar cells in the healthy and only bipolar cells in the degenerated retina. Furthermore, both the photovoltaic and visual STA time courses had no significant deflection from the average gray level up until about a few hundred milliseconds before the spike. This suggests that RGC spiking activity is affected only by the most recent changes in the stimulus. Such short "memory" is another essential feature of prosthetic vision enabling responses to a rapidly changing visual stimulus.

One distinct feature of the photovoltaic STA was three and sometimes four or five (Figure 3.3.2c) peaks in the time course, while visual time courses have only two peaks. The STA convolution with the stimulus predicts the linear portion of the RGC response in a linear-nonlinear model (LNM) of the retina (10). Therefore, the first peak before the spike determines the sign of the preferred change of light level. The second peak of the opposite sign, in turn, predicts how transient the response of the cell will be to a light step of the preferred polarity (11). Thus, the LNM predicts that

the spike rate of the RGC will increase and then decrease in response to the preferred direction of the light level change. More than two peaks suggest that RGC will increase and decrease its spike rate more than once in response to the same stimulus. One possible explanation is that flicker fusion does not happen instantaneously and the response to the change in the NIR pulse amplitude persists for a few pulses following the change. With the pulse frequency matching the white noise movie frame rate, such persistence might explain the multiple peaks we observe in the pSTA time course. Increasing the frequency of the NIR pulses might eliminate this effect, and previous studies showed that frequencies as high as 40Hz can be used (37). Another possible explanation to multiple peaks could be that they represent the sum of the distinct contributions from the bipolar cells and photoreceptors, which occur at different latencies (8).

The opposing center-surround organization we observed in the photovoltaic receptive fields of RGCs in the healthy and in the degenerate retinas is another important feature of retinal processing preserved in prosthetic vision. Receptive field surrounds are thought to contribute to edge detection, and their preservation might result in better prosthetic vision. Two mechanisms are thought to be responsible for the opposing wide surrounds in the visual receptive fields of the healthy retina: (1) negative feedback onto the photoreceptors by the network of the horizontal cells (34; 47), and (2) amacrine cells providing inhibitory inputs to bipolar and ganglion cells (28; 12). Absence of the photoreceptors in the degenerate retina makes it unlikely

that the horizontal cells can contribute to the surrounds we measured in the RCS retina, and therefore amacrine cells are likely to mediate those. Both mechanisms involve the surround signal crossing at least one additional synapse compared to the center signal. We see that the surround signals were indeed somewhat delayed in the visual responses. The surround time course had the first peak earlier before the spike than that of the center (Figure 3.3.4a,b). The coarser time resolution of 20Hz frame rate, compared to 30Hz in the visual stimulus, did not allow us to determine whether this difference was present in the photovoltaic time courses (Figure 3.3.4c,d,e). In healthy visual responses, center and opposing surround have their largest amplitude in the center of the receptive field with the surround spreading further away from the center. Our measurements are consistent with the same spatial dependence of the photovoltaic center and surround responses.

3.3.7 Implications of selective activation of ON and OFF pathways

The distinctly different responses of the ON- and OFF-center RGCs to photovoltaic stimulation in healthy retina can be readily explained by electrical depolarization of the photoreceptors, which elicit responses opposite to hyperpolarization of photoreceptors under visible light. This explanation is supported by the absence of photovoltaic OFF responses in RCS retina and by the elimination of the photovoltaic OFF responses upon pharmacological blockade of neural transmission from photoreceptors to ON-bipolar cells. Our results are consistent with previous findings

that ON and OFF RGCs in healthy rabbit retina can be activated by the opposite phases of a sinusoidal electrical stimulus, and that the response of the ON RGCs disappears when the photoreceptor to ON bipolar cells transmission is selectively blocked (12). It was also shown in the healthy mouse retina that the network-mediated component of ON and OFF RGCs responses to temporally white Gaussian electrical noise delivered epiretinally have distinct STA time courses (55). As a result, it becomes clear that electrical stimulation of photoreceptors preserves the two major retinal pathways, only operating in reversed polarity: ON becoming OFF and vice-versa compared to visual responses. Since this selectivity disappears with the photoreceptor degeneration, it might be useful only during the limited time window when patients lose outer segments, but the cone nuclei are still present. However, even in this case, subretinal implants block the supply of nutrients from the choroid to the retina, which quickly eliminates the remaining photoreceptor somas (40; 37; 36; 38). Epiretinal implants do not have such an effect. Long (≥25ms) electrical pulses delivered by an epiretinal implant have been shown to elicit selective network responses (65). If stimulation of photoreceptors without activation of the RGCs and bipolar cells were possible, it could take advantage of the selective activation of the ON and OFF retinal pathways while some photoreceptor somas are still present in the degenerating retina.

4 Conclusions

4.1 Conclusions

The photovoltaic subretinal prosthesis presented here has undergone several iterations in design leading up to this point. To achieve this new level of spatial resolution and efficiency in delivery of visual information took many years of hard work by dedicated researchers across various fields. I contributed to this work by performing and assisting with roughly ninety experiments, designing custom software in Java and MATLAB for data analysis, performing data analysis, and writing publications. This work was crucial to gain a better understanding of the *in-vitro* performance of the prosthesis before undergoing clinical trials. In particular, we sought to better understand the prosthesis system's level of visual acuity, contrast sensitivity, and ability to resolve dynamic, real-world scenes, as well as selecting between various design iterations of the device which had different-sized pixels and different numbers of photodiodes. The latest iteration of the device with small 70 µm pixels and 2 photodiodes in series per pixel obtained a spatial resolution of 67 µm on the retina, which should correspond to 20/250 vision, which is well below the legal blindness limit of 20/400 as defined by the World Health Organization. The contrast sensitivity thresholds of 55-80% are comparable to other retinal prostheses, and

indicates the need for additional preprocessing to enhance contrast before the image is delivered to the retina. The ability to discern the high-frequency stimulus of at least 20Hz in-vitro and 40Hz in-vivo is new and noteworthy, and markedly better than the 7Hz carrier frequency employed by the only retinal prosthesis currently on the market (ARGUS II epiretinal system).

4.2 Spatial resolution improvement

To increase the spatial resolution even further, the size of the individual pixels must be decreased. The factor limiting this approach is that with smaller pixels, more light is required for stimulation since there will be a smaller light-sensitive portion on each photodiode, and the amount of light delivered to the retina is limited by ocular safety considerations (discussed in Chapter 1.7). However, even with the implementation of smaller pixels, the degree to which the retina can take advantage of higher resolution stimulation is not clear, because the subretinal layer where the device is located is still some tens of microns away from the INL where the bipolar cell layer is stimulated.

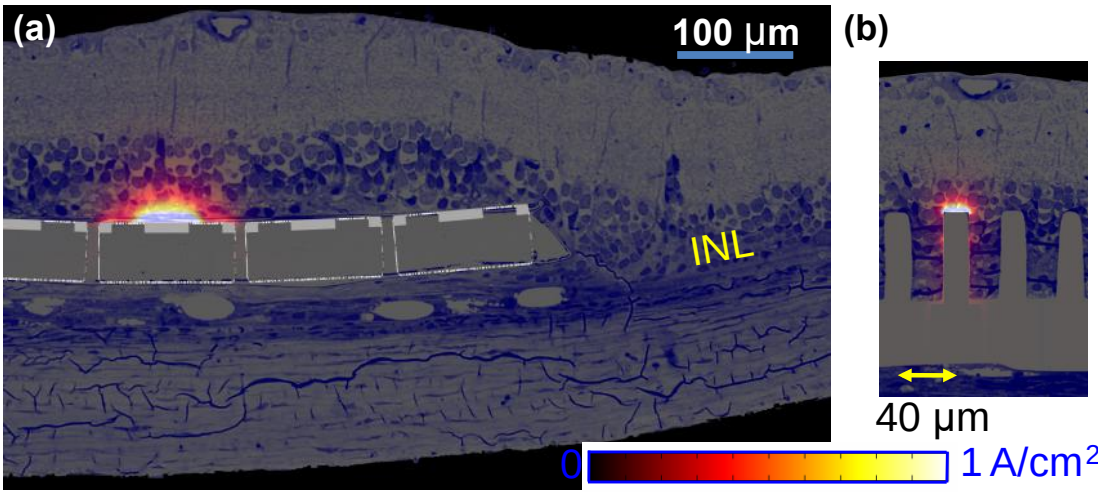

Figure 4.2 (a) Retinal histology of a flat polymer implant in the subretinal space of an RCS rat, with the numerically calculated current distribution from a 115 µm pixel (pixel schematics overlaid). (b) Retinal histology of a pillar array implant, overlaid with the numerically calculated current distribution from electrodes placed on the tops. Implants with pixel densities greater than 256 pixels/mm^2 will likely require the use of such 3-D geometries to achieve sufficient proximity to target neurons.

More localized stimulation, (Figure 4.2b) in the form of deeper penetration into the inner nuclear layer, is likely required to achieve higher levels of spatial resolution, as the current approach results in the stimulating electrodes being located several tens of microns away form the cell bodies that they are stimulating. An alternative approach currently in development at Stanford is a design where each pixel has a small "chimney" which penetrates closer to the bipolar cell layer, and upon which the stimulating electrode is located. Such localized stimulation should help bypass the

problem of overlapping electrical signals from distant smaller pixels, and allow for the possibility of higher visual acuity.

4.3 Human clinical trials

Starting later this year, human clinical trials will begin with Pixium Vision in Paris, France. Currently, the only other FDA-approved retinal prosthesis is the ARGUS II epiretinal implant, which has already begun allowing blinded humans to see again, some of them for the first time in decades. The prosthesis presented here promises to improve on that system in a number of ways including better spatial resolution, a capability for higher-frequency image delivery, easier implantation with wireless power delivery, and the ability to use natural eye movements to determine image location on the retina rather than relying on additional eye-tracking technology.

4.4 Final words

The eye and retina have evolved over millions of years to be very efficient at what they do, and are some of our most important sensory organs. It is difficult to engineer an electrical system that can approach the level of detail that the dense photoreceptors of the fovea region of the human eye are capable of discerning. Perhaps in the near future, as nanotechnology practices continue to deepen, we will approach a level of sophistication where the resolution of retinal prostheses can

match that of the healthy retina. The location of electrical stimulation as well as the density of possible stimulation points will determine how efficiently a prosthetic device is able to take advantage of the existing retinal circuitry remaining after photoreceptor degradation. Of course, an even better solution will be to prevent photoreceptor degradation in the first place, or to replace the missing photoreceptors with new cell growth. Several developing technologies in the field of stem-cell therapy, discussed in Chapter 1, give hope for more natural forms of treatments such as these. It is hard to imagine a better system for vision than the one developed through millions of years of evolution and therefore it is likely that the preferred therapy for restoration of sight will ultimately be based on regrowth of the original cells. Due to some of the current limitations on such research, (also discussed in Chapter 1), it is likely that retinal prostheses will continue to be of enormous benefit for sight-impaired patients for decades to come.

References

[1] Ahuja, A. K., Dorn, J. D., Caspi, A., McMahon, M. J., Dagnelie, G., Dacruz, L., Stanga, P., Humayun, M. S., Greenberg, R. J., and Group, A. I. S. Blind subjects implanted with the argus ii retinal prosthesis are able to improve performance in a spatial-motor task. Br. J. Ophthalmol. 95, 4 (2011), 539-543.

[2] Barlow, H. B., Hill, R. M., and Levick, W. R. Retinal ganglion cells responding selectively to direction and speed of image motion in the rabbit. J. Physiol. 173, 3 (1964), 377-407.

[3] Baylor, D. A., Lamb, T., and Yau, K.-W. The membrane current of single rod outer segments. J. Physiol. 288, (1979), 589-611.

[4] Besch, D., Sachs, H., Szurman, P., Gulicher, D., Wilke, R., Reinert, S., Zrenner, E., Bartz-Schmidt K, U., and Gekeler, F. Extraocular surgery for implantation of an active subretinal visual prosthesis with external connections: easibility and outcome in seven patients. Br. J. Ophthalmol. 92, 10 (2008), 1361-1368.

[5] Boinagrov, D., Lei, X., Goetz, G., Kamins, T., Mathieson, K., Galambos, L., Harris, J., and Palanker, D. V. Photovoltaic pixels for neural stimulation: Circuit models and performance. IEEE Trans. Biomed. Circuits Syst. (2015).

[6] Boinagrov, D., Loudin, J., and Palanker, D. Strength-duration relationship for extracellular neural stimulation: numerical and analytical models. J. Neurophysiol. 104 (2010), 2236-2248.

[7] Boinagrov, D., Pangratz-Fuehrer, S., Goetz, G., and Palanker, D. Selectivity of direct and network-mediated stimulation of the retinal ganglion cells with epi-, sub- and intra-retinal electrodes. J. Neural Eng. 11, 2 (2014), 026008.

[8] Caldwell, J., and W., D. N. New properties of rabbit retinal ganglion cells. J. Physiol. (Lond.) 276 (1978), 257-276.

[9] Chang, B., Hawes, N. L., Hurd, R. E., Davisson, M. T., Nusinowitz, S., and Heckenlively, J. R. Retinal degeneration mutants in the mouse. Vision Res. 42 (2002), 517525.

[10] Chichilnisky, E. J. A simple white noise analysis of neuronal light responses. Network: Comput. Neural Syst. 12 (2001), 199-213.

[11] Chichilnisky, E. J., and Kalmar, R. S. Functional asymmetries in on and off ganglion cells of primate retina. J. Neurosci. 22, 7 (2002), 2737-2747.

[12] Cook, P.B., P.D. Lukasiewicz, and J.S. McReynolds, Action Potentials Are Required for the Lateral Transmission of Glycinergic Transient Inhibition in the Amphibian Retina. The Journal of Neuroscience, 18, 6 (1998). 2301-2308.

[13] da Cruz, L., Coley, B. F., Dorn, J., Merlini, F., Filley, E., Christopher, P., Chen, F., Wuyyuru, V., Sahel, J., Stanga, P., Humayun, M., Greenberg, R. J., and Dagnelie G.; for the Argus II Study Group . The argus ii epiretinal prosthesis system allows letter and word reading and long-term function in patients with profound vision loss. Br. J. Ophthalmol. 67 , 5 (2013), 632-636.

[14] Dacey, D. M. Origins of perception: retinal ganglion cell diversity and the creation of parallel visual pathways . MIT Press, 2004, pp. 281-301.

[15] Dean, P. Visual pathways and acuity in hooded rats. Behavioural Brain Research 3 , 2 (1981), 239-271.

[15] Delori, F. C., Webb, R. H., and Sliney, D. H. Maximum permissible exposures for ocular safety (ansi 2000), with emphasis on ophthalmic devices. J. Opt. Soc. Am. 24, 5 (2007).

[17] Derrington, A. M., and Lennie, P. Spatial and temporal contrast sensitivities of neurons in lateral geniculate nucleus of macaque. J Physiol. 357 (1984), 219-240.

[18] Devries, S. H., and Baylor, D. A. Mosaic arrangement of ganglion cell receptive fields in rabbit retina. Journal of Neurophysiology 78, 4 (1997), 2048-2060.

[19] Enroth-Cugell, C., and Robson, J. G. The contrast sensitivity of retinal ganglion cells of the cat. J. Physiol. 187 (1966), 517-552.

[20] Field, G., and Chichilnisky, E. Information processing in the primate retina: Circuitry and coding. Annual Review of Neuroscience 30, 1 (2007), 1-30.

[21] Flores, T., et al., Optimization of Return Electrodes in Neurostimulating Arrays. J Neural Eng, 2016. in print.

[22] Freeman, D.K. and S.I. Fried, Multiple components of ganglion cell desensitization in response to prosthetic stimulation. J Neural Eng, 8, 1 (2011). 016008.

[23] Goetz, G., Smith, R., Lei, X., Galambos, L., Kamins, T., Mathieson, K., Sher, A., and Palanker, D. Contrast Sensitivity With a Subretinal Prosthesis and Implications for Efficient Delivery of Visual Information. Invest Ophthalmol Vis Sci, 56, 12, (2015). 7186-7194.

[24] Hafed, Z. M., Stingl, K., Bartz-Schmidt, K.U., Gekeler F., and Zrenner, E. Oculomotor behavior of blind patients seeing with a subretinal visual implant. Vision Res. 118, (2016), 119-31.

[25] Harnois, C., Bodis-Wollner, I., and Onofrj, M. The effect of contrast and spatial frequency on the visual evoked potential of the hooded rat. Exp. Brain Res. 57 (1984), 1-8.

[26] Heine, W., and Passaglia, C. Spatial receptive field properties of rat retinal ganglion cells. Visual Neurosci. 28, 05 (2011), 403-417.

[27] Hodgkin, A. L., and Huxley, A. F. A quantitative description of membrane current and its application to conduction and excitation in nerve. J. Physiol. 117, 4 (1952), 500544.

[28] Ichinose, T. and P.D. Lukasiewicz, Inner and outer retinal pathways both contribute to surround inhibition of salamander ganglion cells. J Physiol, 565 pt 2, (2005), 517-535.

[29] Jensen, R. J., and Rizzo, J. F. Thresholds for activation of rabbit retinal ganglion cells with a subretinal electrode. Exp Eye Res 83, 2 (2006), 367-73.

[30] Jepson, L. H., Hottowy, P., Mathieson, K., Gunning, D. E., Dabrowski, W., Litke, A. M., and Chichilnisky, E. J. Focal electrical stimulation of major ganglion cell types in the primate retina for the design of visual prostheses. J. Neurosci. 33, 17 (2013), 7194-205.

[31] Joucla, S. and B. Yvert. Improved Focalization of Electrical Microstimulation Using Microelectrode Arrays: A Modeling Study. PLoS ONE, (2009), 4 (3): p. e4828.

[32] Kolb, H., Mariani, A., and Gallego, A. A second type of horizontal cell in the monkey retina. J. Comp. Neurol. 189 (1980), 31-44.

[33] Kuffer, S. W. Discharge patterns and functional organization of mammalian retina. J. Neurophysiol. 16 (1953), 37-68.

[34] Li, P. H., Gauthier, J. L., Schiff, M., Sher, A., Ahn, D., Field, G. D., Greschner, M., Callaway, E. M., Litke, A. M., and Chichilnisky, E. J. Anatomical identification of extracellularly recorded cells in large-scale multielectrode recordings. J. Neurosci. 35, 11 (2015), 4663-75.

[35] Litke, A. M., Bezayiff, N., Chichilnisky, E. J., Cunningham, W., Dabrowski, W., Grillo, A. A., Grivich, M. I., Grybos, P., Hottowy, P., Kachiguine, S., Kalmar, R. S., Mathieson, K., Petrusca, D., Rahman, M., and Sher, A. What does the eye tell the brain? Development of a system for the large-scale recording of retinal output activity. IEEE Trans. on Nuclear Science 51 , 4 (2004), 1434-1440.

[36] Lorach, H., Goetz, G., Mandel, Y., Lei, X., Kamins, T. I., Mathieson, K., Huie, P., Dalal, R., Harris, J. S., and Palanker, D. Performance of photovoltaic arrays in-vivo and characteristics of prosthetic vision in animals with retinal degeneration. Vision Res. (2014).

[37] Lorach, H., Goetz, G., Smith, R., Lei, X., Mandel, Y., Kamins, T., Mathieson, K., Huie, P., Harris, J., Sher, A., and Palanker, D. Photovoltaic restoration of sight with high visual acuity. Nat. Medicine (2015).

[38] Lorach, H., et al., Development of Animal Models of Local Retinal Degeneration. Invest Ophthalmol Vis Sci, 56, 8 (2015). 4644-52.

[39] Loudin, J. D., Cogan, S. F., Mathieson, K., Sher, A., and Palanker, D. V. Photodiode circuits for retinal prostheses. IEEE Trans. Biomed. Circuits Syst. 5 (2011), 468-80.

[40] Mandel, Y., Goetz, G., Lavinsky, D., Huie, P., Mathieson, K., Wang, L., Kamins, T., Galambos, L., Manivanh, R., Harris, J., and Palanker, D. Cortical responses elicited by photovoltaic subretinal prostheses exhibit similarities to visually evoked potentials. Nat. Commun. 4 (2013), 1980.

[41] Marc, R. E., Jones, B. W., Watt, C. B., and Strettoi, E. Neural remodeling in retinal degeneration. Progress in Retinal and Eye Research 22, 5 (2003), 607-655.

[42] Masland, R. H. The fundamental plan of the retina. Nat. Neurosci. 4, 9 (2001), 877-886.

[43] Masland, R. H. "The tasks of amacrine cells". Visual neuroscience. 29, 1 (2012) 3–9.

[44] Mathieson, K., Loudin, J., Goetz, G., Huie, P., Wang, L., Kamins, T. I., Galambos, L., Smith, R., Harris, J. S., Sher, A., and Palanker, D. Photovoltaic retinal prosthesis with high pixel density. Nat. Photonics 6, 6 (2012), 391-397.

[45] Mazzoni, F., Novelli, E., Strettoi, E. Retinal ganglion cells survive and maintain normal dendritic morphology in a mouse model of inherited photoreceptor degeneration. J Neurosci 28, 52 (2008), 14282–14292.

[46] McCamy, M. B., Otero-Millan, J., Macknik, S. L., Yang, Y., Troncoso, X. G., Baer, S. M., Crook, S. M., and Martinez-Conde, S. Microsaccadic eficacy and contribution to foveal and peripheral vision. J. Neurosci. 32, 27 (2012), 9194-204.

[47] McMahon, M.J., O.S. Packer, and D.M. Dacey, The classical receptive field surround of primate parasol ganglion cells is mediated primarily by a non-GABAergic pathway. J Neurosci, 24, 15, (2004) 3736-45.

[48] Mikami, A., Newsome, W. T., and Wurtz, R. H. Motion selectivity in macaque visual cortex. ii. spatiotemporal range of directional interactions in mt and v1. J. Neurophysiol. 55, 6 (1986), 1328-1339.

[49] Nanduri, D., Fine, I., Horsager, A., Boynton, G. M., Humayun, M. S., Greenberg, R. J., and Weiland, J. D. Frequency and amplitude modulation have different effects on the percepts elicited by retinal stimulation. Investigative Ophthalmology & Visual Science 53, 1 (2012), 205-214.

[50] Petrusca, D., Grivich, M. I., Sher, A., Field, G. D., Gauthier, J. L., Greschner, M., Shlens, J., Chichilnisky, E. J., and Litke, A. M. Identification and characterization of a y-like primate retinal ganglion cell type. J. Neurosci. 27, 41 (2007), 11019-27.

[51] Pillow, J. W., Shlens, J., Paninski, L., Sher, A., Litke, A. M., Chichilnisky, E. J., and Simoncelli, E. P. Spatio-temporal correlations and visual signalling in a complete neuronal population. Nature 454, 7207 (2008), 995-999.

[52] Prusky, G. T., West, P. W. R., and Doublas, R. M. Behavioral assessment of visual acuity in mice and rats. Vision Res. 40 (2000), 2201-2209.

[53] Rieke, F., and Baylor, D. A. Single-photon detection by rod cells of the retina. Reviews of Modern Physics 70, 3 (1998), 1027-36.

[54] Schraermeyer, U., Thumann, G., Luther, T., and Kociok, N. Subretinally transplanted embryonic stem cells rescue photoreceptor cells from degeneration in the RCS rats. Cell Transplant 10 (2011), 673-680.

[55] Sekhar, S., et al., Tickling the retina: integration of subthreshold electrical pulses can activate retinal neurons. J Neural Eng, 13, 4, (2016). 046004.

[56] Sekirnjak, C., Hottowy, P., Sher, A., Dabrowski, W., Litke, A. M., and Chichilnisky, E. J. Electrical stimulation of mammalian retinal ganglion cells with multielectrode arrays. J. Neurophysiol. 95, 6 (2006), 3311-27.

[57] Smith, W., Assink, J., Klein, R., Mitchell, P., Klaver, C. C., Klein, B. E., Hofman, A., Jensen, S., Wang, J. J., and de Jong, P. T. Risk factors for age-related macular degeneration: Pooled findings from three continents. Ophthalmology 108, 4 (2001), 697-704.

[58] Smith, R., Goetz, G., Ho, E., Lei, X., Galambos, L., Kamins, T., Mathieson, K., Palanker, D, and Sher, A. Spatio-temporal characteristics of retinal response to network-mediated photovoltaic stimulation. Currently in submission process to J Neurophysiology.

[59] Stingl, K., Bartz-Schmidt, K. U., Besch, D., Braun, A., Bruckmann, A., Gekeler, F., Greppmaier, U., Hipp, S., Hortdorfer, G., Kernstock, C., Koitschev, A., Kusnyerik, A., Sachs, H., Schatz, A., Stingl, K. T., Peters, T., Wilhelm, B., and Zrenner, E. Artificial vision with wirelessly powered subretinal electronic implant alpha-ims. Proc. Biol. Sci. 280, 1757 (2013), 20130077.

[60] Stingl, K., Bartz-Schmidt, K.-U., Gekeler, F., Kusnyerik, A., Sachs, H., and Zrenner, E. Functional outcome in subretinal electronic implants depends on foveal eccentricity. Invest. Ophth. Vis. Sci. 54, 12 (2013), 7658-7665.

[61] Thibos L., and Werblin F.S. The response properties of the steady antagonistic surround in the mudpuppy retina. J Physiol. 278 (1978), 79–99.

[62] van Alphen, B., Winkelman, B. H., and Frens, M. A. Age- and sex-related differences in contrast sensitivity in c57bl/6 mice. Invest. Ophthalmol. Vis. Sci. 50, 5 (2009), 2451-8.

[63] Victor, J. D., and Shapley, R. M. The nonlinear pathway of y ganglion cells in the cat retina. J. Gen. Physiol. 74, 6 (1979), 671-689.

[64] Wassle, H. Parallel processing in the mammalian retina. Nat. Rev. Neurosci. 5, 10 (2004), 747-757.

[65] Weitz, A.C., et al., Improving the spatial resolution of epiretinal implants by increasing stimulus pulse duration. Science Translational Medicine, 7. 318, (2015). 318ra203.

[66] Werblin, F.S. and J.E. Dowling, Organization of the retina of the mudpuppy, Necturus maculosus. II. Intracellular recording. J Neurophysiol, 32, 3 (1969). 339-355.

[67] Yizhar, O., Fenno, L. E., Davidson, T. J., Mogri, M., and Deisseroth, K. Optogenetics in neural systems. Neuron 71, 1 (2011), 9-34.

[68] You, Y., Klistorner, A., Thie, J., and Graham, S. Latency delay of visual evoked potential is a real measurement of demyelination in a rat model of optic neuritis. Invest. Ophth. Vis. Sci. 52, 9 (2011), 6911-6918.